Spring 2-12-2019

Melt Inclusions and Their Application - New Perspective on the Subsurface Architecture of Cerro Negro Volcano, Nicaragua

John M. Hamilton
University of New Mexico - Main Campus

John M Hamilton
Candidate

Earth and Planetary Sciences
Department

This thesis is approved, and it is acceptable in quality and form for publication:

Approved by the Thesis Committee:

Tobias Fischer, Chairperson

Jin Zhang

Joseph Galewsky

Melt Inclusions and Their Application - New Perspective on the Subsurface Architecture of Cerro Negro Volcano, Nicaragua

by

John Hamilton

Bachelor of Science Geology, with Honors

Bachelor of Science Chemistry

University of Washington

THESIS

Submitted in Partial Fulfillment of the Requirements for the Degree of

Master of Science

Earth and Planetary Sciences

The University of New Mexico

Albuquerque, New Mexico

May 2019

Acknowledgements

I want to thank all my friends and family for all their support and encouragement throughout this educational process. I appreciate my fellow graduate students that have helped me with classes, rehearsals, and brainstorming in completing this thesis.

I especially want to thank my father, Roy R. Hamilton who always supported any decision that I made and would have done the same with this change in career late in life. I wish he could be here to see my growth and completion, but I know he is still alive in my heart. I would also like to thank my partner Brian Ross for allowing me to choose this educational path without ever complaining during the tough times. I never could have completed this without his support.

I want to thank Cindy Jaramillo, Faith Mutchnik, Paula Pascetti, and Mabel Chavez in the Earth and Planetary Science Department for helping with any questions, arranging travel, and getting reimbursements processed quickly so I never had to worry.

I want to thank Dr. Mike Spilde for his expertise in utilizing the microprobe and Dr. Dawnika Blatter at USGS in Menlo Park for the fantastic assistance in obtaining my FTIR data.

I would like to thank my committee members, Dr. Jin Zhang and Dr. Joseph Galewsky for allowing me to let the project evolve as it has and lending their expertise where needed.

I am especially thankful to my advisor Dr. Tobias Fischer who has allowed me to develop this project and reach a conclusion we did not originally hypothesize. I appreciate all his support and guidance, passion for the field, and desire for the greatest success of his students. I have learned so much in the past two years and I look forward to the next step in this educational process under his advisement.

Melt Inclusions and Their Application - New Perspective on the Subsurface Architecture of Cerro Negro Volcano, Nicaragua

John Hamilton

B.S., Geology, University of Washington, 2016

B.S., Chemistry, University of Washington, 2016

M.S., Earth and Planetary Sciences, University of New Mexico, 2019

ABSTRACT

Volatiles are the drivers of volcanic eruptions and monitoring and measurement in quiescent times are the key in determining when unrest within a volcanic system is beginning leading to possible cataclysms. Previous studies have focused on direct measurements from volcanic plumes or fumaroles, however, this study proposes the use of melt inclusions from tephra to determine volatile contents from the 1992 eruption of Cerro Negro Volcano, Nicaragua. The analysis of melt inclusions adds a new technique to the volatile analytical toolbox and can help to determine volatile contents from past eruptions and their subsequent evolution within a volcanic system.

Though melt inclusions are easier to sample than direct degassing and ideally represent the undegassed magma at depth, they are not without complications. Vapor bubbles are almost ubiquitous within all melt inclusions and potentially contain up to 100% of the original carbon dioxide content at entrapment. If the carbon dioxide content within the vapor bubble is not considered, initial volatile content will be highly underestimated and thus depth of entrapment could be off by several kilometers. Additionally, the miscalculated carbon dioxide concentrations lead to errors in other ratios that help to determine the state of the volcanic system prior to and during eruptive events.

This study will focus on determining the corrected carbon dioxide contents of melt inclusions from the 1992 erupted tephra to visualize a new subsurface architecture of Cerro Negro volcano compared to previous studies that show magma holding bodies at shallow depths. By correcting for the carbon dioxide contents within the bubble, a new schematic of the Cerro Negro plumbing system will be presented that comprises multiple interconnected magma lenses at greater depths than previously presented. This blueprint is normally suggested for spreading centers, however, this study will show that Cerro Negro is the optimal example of an arc volcano containing this subsurface architecture.

Table of Contents

1.0 Introduction

Volcanology has progressively moved from a qualitative to quantitative discipline, however, understanding the plumbing system beneath volcanic complexes remains problematic. The processes at depth that cause these large edifices to produce sometimes cataclysmic eruptions continues to be explored to improve our knowledge of what makes these systems propagate and to help improve hazard mitigation for those living near these settings. Various techniques have been employed to help answer questions of how these volcanic systems operate at the subsurface and this study will explore the analysis of volatiles utilizing melt inclusion within tephra from the 1992 Strombolian eruption at Cerro Negro in Nicaragua to better envision the subsurface architecture. This is a departure from previous studies that utilize fumarole gases for volatile analysis and adds a different technique to the toolbox when fumarole sampling may not be adequate or accessible.

When picturing the subsurface of a volcanic complex, the traditional view is a magma chamber located at a particular depth connected to the open air crater via a conduit as shown in Figure 1. This is especially true in arc volcanic settings, where magma chambers are typically located at 3-6 km depth connected to the surface via a fluid-filled conduit only during eruptions, though in some settings, magma may ascend directly from the mantle without being stored in the crust (National Academies of Science, Engineering, and Medicine, 2017). Though systems like this exist, it is hard to conceive that all magmatic systems follow this subsurface blueprint. There is growing evidence that magma reservoirs may comprise an interconnected complex of vertical and/or horizontal magma-filled cracks, or interleaved lenses of magma and solid material

(Cashman and Giordano, 2014). Additionally, it is likely that some arc volcanoes have storage bodies in the 3-6 km range, however, the deepest structure beneath volcanoes is less well constrained. Swarms of low-frequency earthquakes at mid to lower-crustal depths (10-40 km) beneath volcanoes suggest that fluid is periodically transferred into the base of the crust (Power et al., 2004). Through the analysis of volatile concentrations contained in melt inclusions from the 1992 Cerro Negro eruption, the possibility of a subsurface constructed of magma lenses at discrete depths exceeding 3-6 km will be explored.

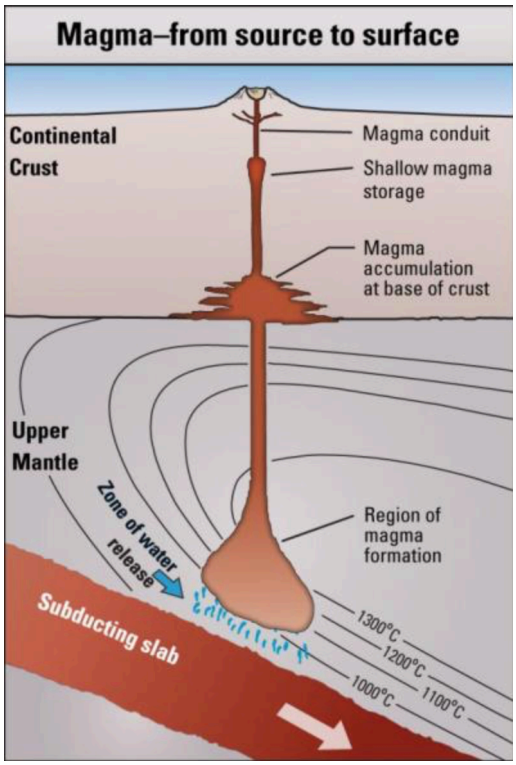

Figure 1 - Traditional schematic of the subsurface of a volcanic system (USGS).

Melt inclusions are small volumes of melt that are trapped inside phenocrysts at depth prior to eruption shown in Figure 2. The host crystal will act as a tiny pressure vessel allowing melt inclusions to remain at higher pressure than the ambient melt surrounding the crystal as the magma ascends and eventually erupts quenching to glass.

Thus, analysis of melt inclusions can potentially provide a record of magmatic conditions, including dissolved volatile components, at the time of crystal growth (Lowenstern, 1995; Danyushevsky et al., 2002; Metrich and Wallace, 2008, Wallace et al., 2015). In particular, carbon dioxide contents within the melt inclusion record changes in depth of formation due to its high insolubility within the magma that quickly decreases upon ascent depressurization acting as a geobarometer. Conversion of the carbon dioxide concentrations to pressures and thus depth give a more accurate formation location at depth compared to fumarole gas analysis, especially at locations where low-temperature fumaroles exist. Low-temperature fumarole gases measured at the surface have decoupled from the magma undergoing reactions with wall rock and/or water as it ascends. Therefore, low-temperature fumarole gases show volatile concentrations that are not representative of the magmatic gas, while melt inclusions ideally sample the magmatic gas content at the resident depth. Though the information obtained in relation to carbon dioxide from melt inclusions is valuable, melt inclusions do not necessarily record all volatiles during crystallization and/or decompression (Iacovino, 2015) primarily due to the presence of a nearly ubiquitous vapor bubble within the melt inclusion.

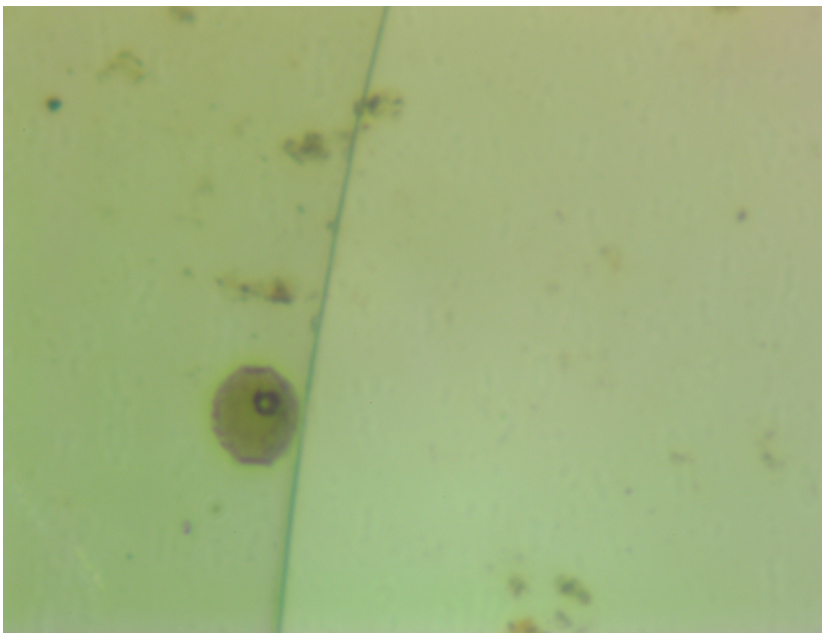

Figure 2 - Melt inclusion with accompanying vapor bubble contained within a host olivine crystal from the 1992 eruption at Cerro Negro.

The formation of a bubble in a melt inclusion after trapping is a natural consequence of the pressure-volume-temperature properties of crystal-melt-volatile systems. Following entrapment, as the host phenocryst and its associated melt inclusion cool, the volume occupied by the melt inclusion will decrease more than that of the host crystal due to different thermal expansion properties. If the melt present cannot remain metastable (Lowenstern, 1995) during initial cooling, a bubble forms in the melt inclusion as a necessary response to these processes (Roedder 1979, 1984; Moore et al., 2015). The end result is that to determine the initial carbon dioxide concentration of the entire melt inclusion at time of entrapment at depth involves adding back the amount of carbon dioxide in the vapor bubble. If the concentration within the bubble is not considered, which could be up to 100% of the total carbon dioxide content, trapping pressures can be underestimated by several kilometers, therefore, this calculation will be a priority in this study.

Analyses using micro-reflectance FTIR, microprobe analysis, pressure-temperature modeling and the Redlich-Kwong equation will be employed to determine melt inclusion composition as well as volatile contents within the melt inclusion and vapor bubble. Synthesis of this data will lead to a hypothesis of the plumbing system at Cerro Negro that deviates from the traditional magma chamber linked to the surface, but instead explore a system of subsurface magma lenses that all contributed to the 1992 VEI 3 eruption.

2.0 Background

2.1 Geologic Setting

Cerro Negro is the youngest volcano along the Central American Volcanic Belt (CAVB) (Venugopal et al., 2016) where the Cocos Plate subducts beneath the Caribbean Plate (Figure 3).

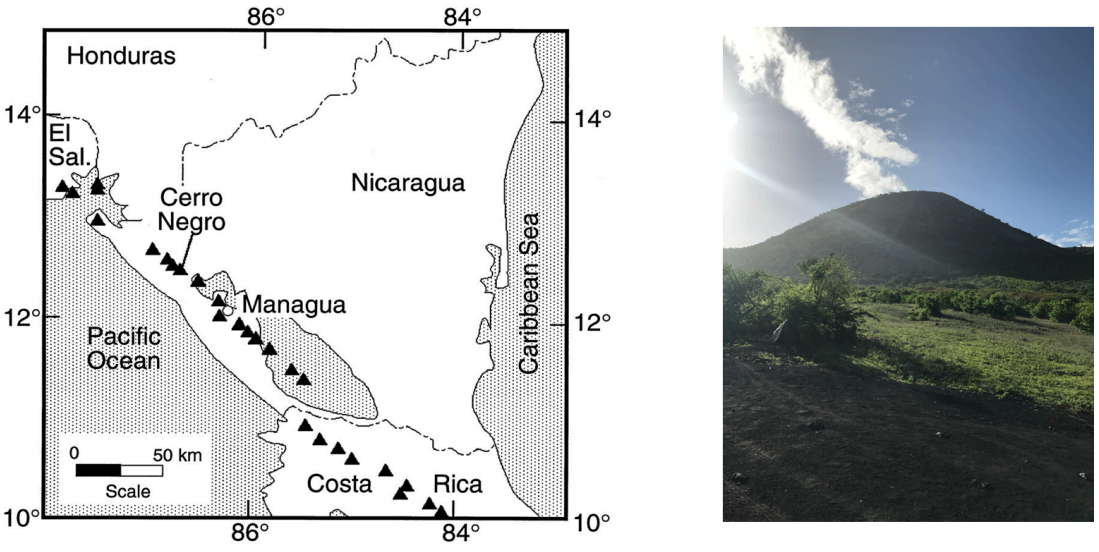

Figure 3 - Map displaying the location of Cerro Negro within the Central American Volcanic Belt from Roggensack et al., 1997 (left). Photo taken of Cerro Negro before ascent (right).

The Central American subduction zone is characterized by rapid (70–90 mm/year) convergence of young (15–25 Ma) oceanic lithosphere (Barckhausen et al., 2001; DeMets, 2001) with the steepest angle of subduction along the CAVB at approximately 75^{o} - 80^{o} (Funk et al., 2009) off the Nicaraguan coast. Cerro Negro erupts basaltic lava compared to the felsic stratovolcanoes to the northwest and southeast giving Cerro Negro its black appearance within the Nicaraguan volcanic range. Though presently listed as a polygenetic cinder cone (Venugopal et al., 2016), the magma production rate for Cerro Negro (~1.6 km^3/k.v.) is the same magnitude as those of a variety of composite volcanoes (McKnight & Williams, 1997).

The production of basaltic lavas is aided by the tectonic setting of the region. The relatively thin crust in Nicaragua and the N-S striking extensional structures that cross the volcanic front (Figure 4) promote rapid transit of magmas through the crust, allowing less fractionated basalts to erupt and minimizing hybridization of the different magma types (Carr et al., 2013). These primitive magmas are the result of dikes paralleling the NNW extensional regime (La Femina et al., 2002) and thus, where the crust is thinner in Nicaragua, mafic basalts are abundant (Carr et al., 2013). The volatile concentrations presented below from melt inclusion analysis also show this primitive basalt signature compared to the low-temperature fumarole data that displays a more evolved volatile content.

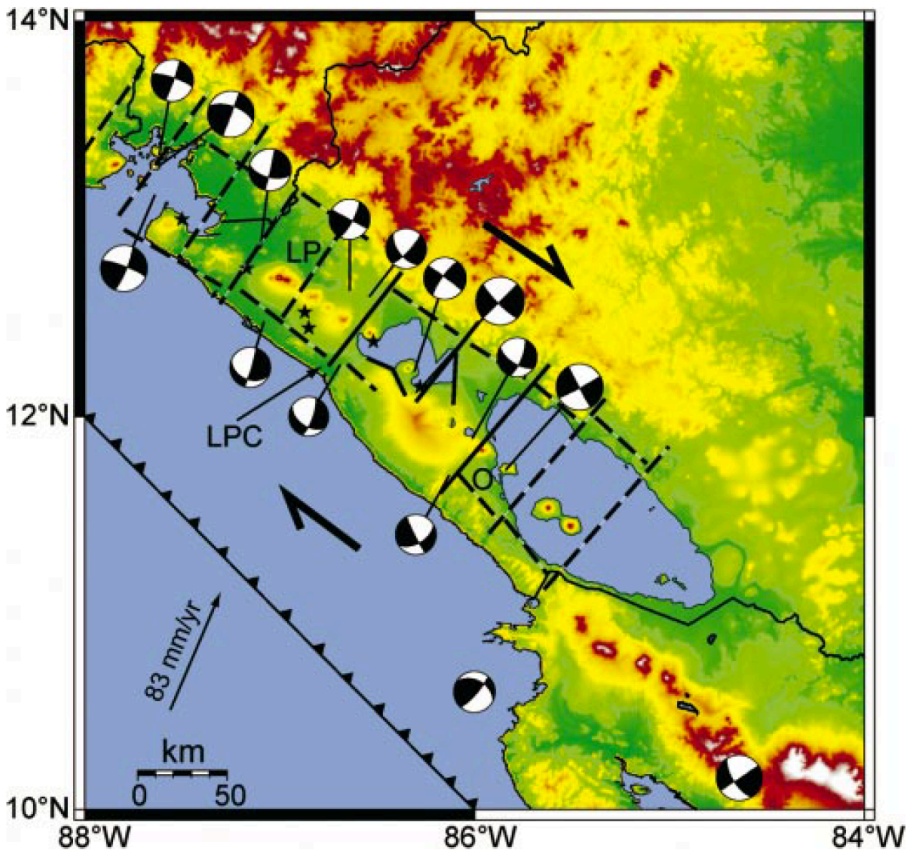

Figure 4 - Schematic representation showing the alignment of faults along the Nicaraguan volcanic front from LaFemina et al., 2002.

2.2 Volcanic History

Cerro Negro is Central America's youngest volcano having erupted for the first time in 1850 and subsequently 22 additional times over its 150-year life (McKnight & Williams, 1997). Cerro Negro produced Strombolian to subplinian type eruptions with intervals of a few years to several decades producing the present 250-m-high basaltic cone (volcano.si.edu). On the volcanic explosivity index (VEI) of Carey and Sigurdsson (1989), the eruptions of Cerro Negro are within the VEI 2 and VEI 3 regions with the more recent explosive eruptions characteristic of VEI 3 type eruptions, producing the most voluminous ash-fall deposit in 1992 (McKnight & Williams, 1997). Cerro Negro's

cone has changed greatly in shape and dimension since its first eruption in 1850 and for most of its existence, has looked more like a small composite volcano than a cinder cone (Figure 5).

Figure 5 - Cerro Negro's black basaltic dome rising from the Nicaraguan vegetated countryside as shown in the Smithsonian Institution Global Volcanism Program database.

2.3 1992 Eruption

The 1992 Strombolian eruption ended a quiescent period of 21 years on April 9, 1992 (Figure 6). The initial explosive phase produced a plume 7-7.5 km high and deposited ash to the W and WSW (Figure 7) before slowing on April 12, 1992 and finally ending on April 14, 1992 (volcano.si.edu). The eruption distributed an estimated 1.7 million tons of ash over a 200 square kilometer area (Malilay et al., 1996). The tephra from this eruption make up the samples collected and processed in the methods section.

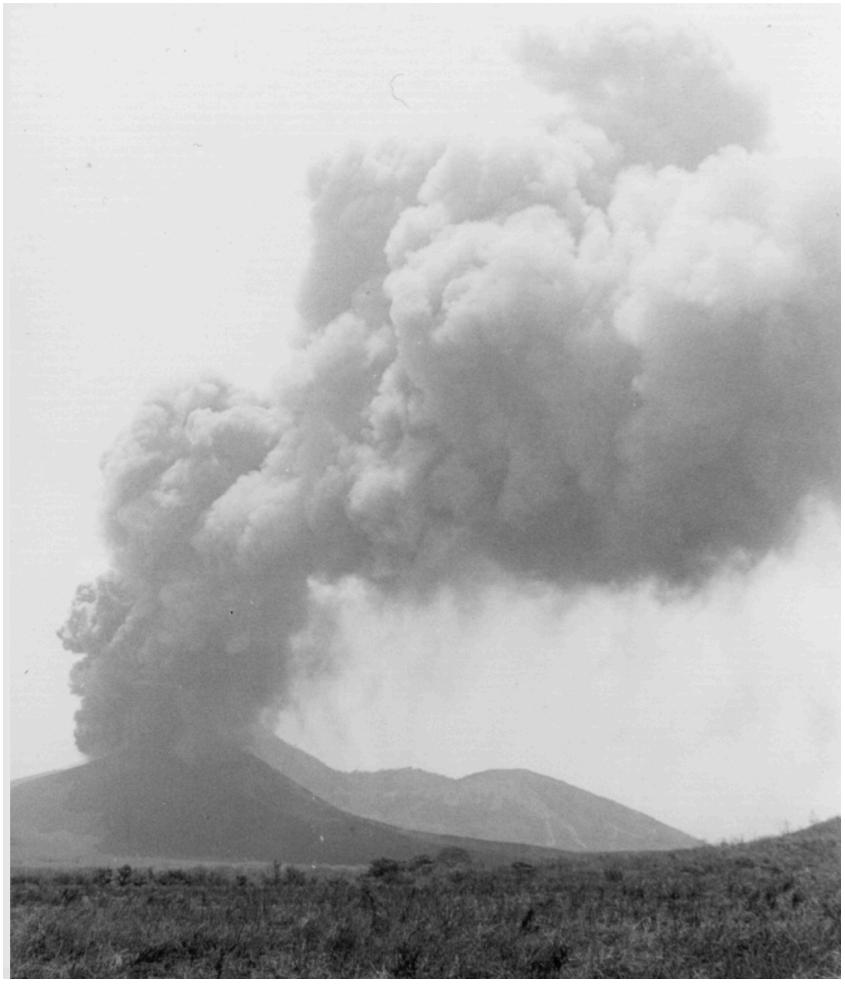

Figure 6 - Photograph of the final stages of Cerro Negro's 1992 eruption on April 14, 1992 courtesy of G. Soto in the Smithsonian Institution Global Volcanism Program database.

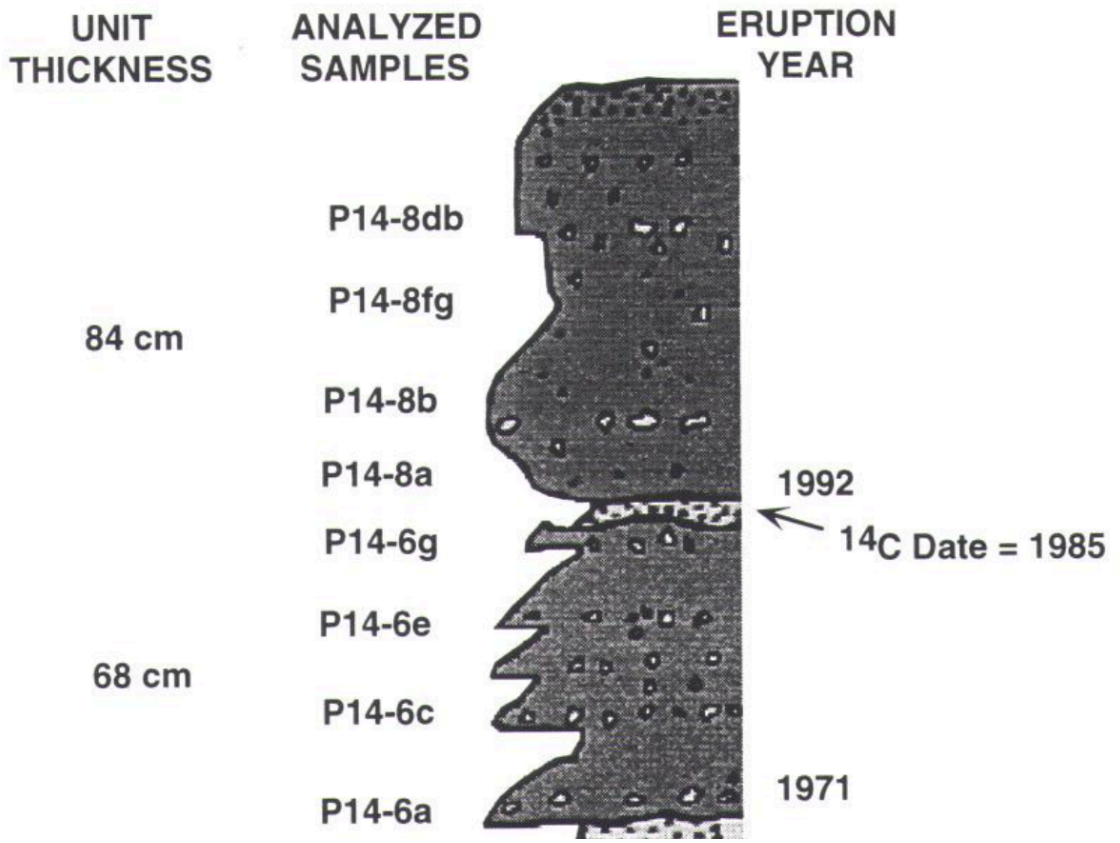

Figure 7 - Tephra column from McKnight (1995) showing the thickness of the 1992 eruption for a pit dug 5 km WSW of Cerro Negro. This pit lies between our sampling sites listed in the methods section.

3.0 Methods

3.1 Sample Collection

Ash samples and fumarole gases were collected from Cerro Negro volcano in Nicaragua on June 1-3, 2017. A map showing previous sampling pit locations from McKnight (1995) (Figure 8) was used to determine potential locations for ash collection WSW of the main vent representing the 1992 eruption.

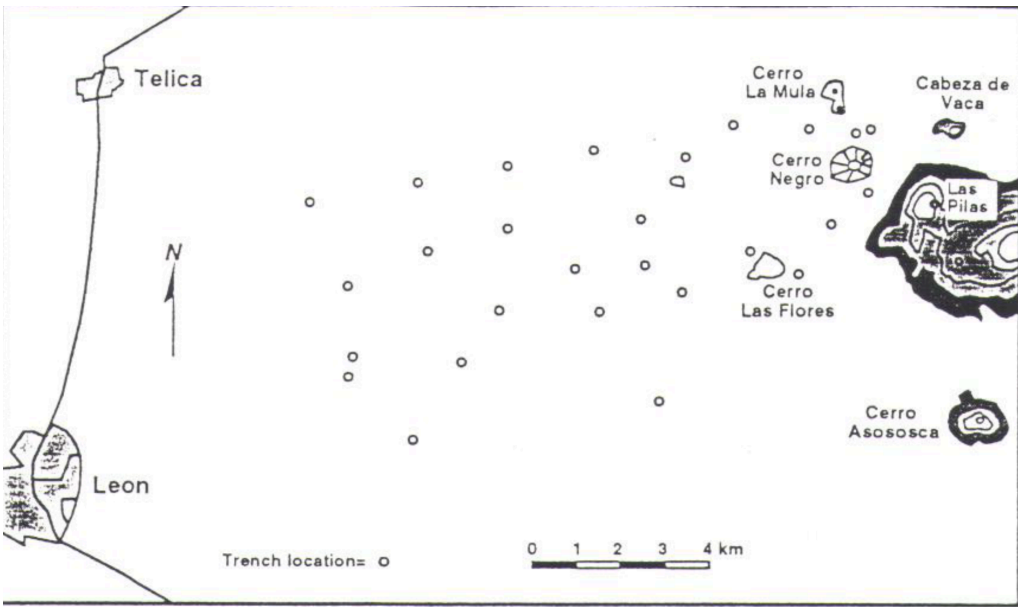

Figure 8 - Map showing ash pits from the 1992 Cerro Negro eruption that were sampled in McKnight's thesis, 1995.

Upon arrival at INETER in Nicaragua, a 2004 thesis by Kristin Martin was provided that showed numerous sampling sites of the 1992 eruption accompanied with latitude and longitude coordinates. From this listing, five sites were chosen (Figures 9, 10, 11) with coordinates and thickness shown in Table 1. Conversions from northing and easting coordinates to latitude and longitude were done using uwgb.edu converter. The 1992 eruption overlies the 1971 eruption and is identifiable as a coarse layer with an abundance of large red lithics (McKnight, 1995) in addition to a soil layer that developed between the 1971 and 1992 eruptions. The soil layer was confirmed at pit 4 where a burned tree was located at the bottom of the pit (Figure 9).

Figure 9 - Base of pit 4 for the 1992 Cerro Negro eruption at 140 cm showing the separation of the 1992 and 1971 tephra layers. Note the abundance of red lithics and soil layer containing the burned tree segment.

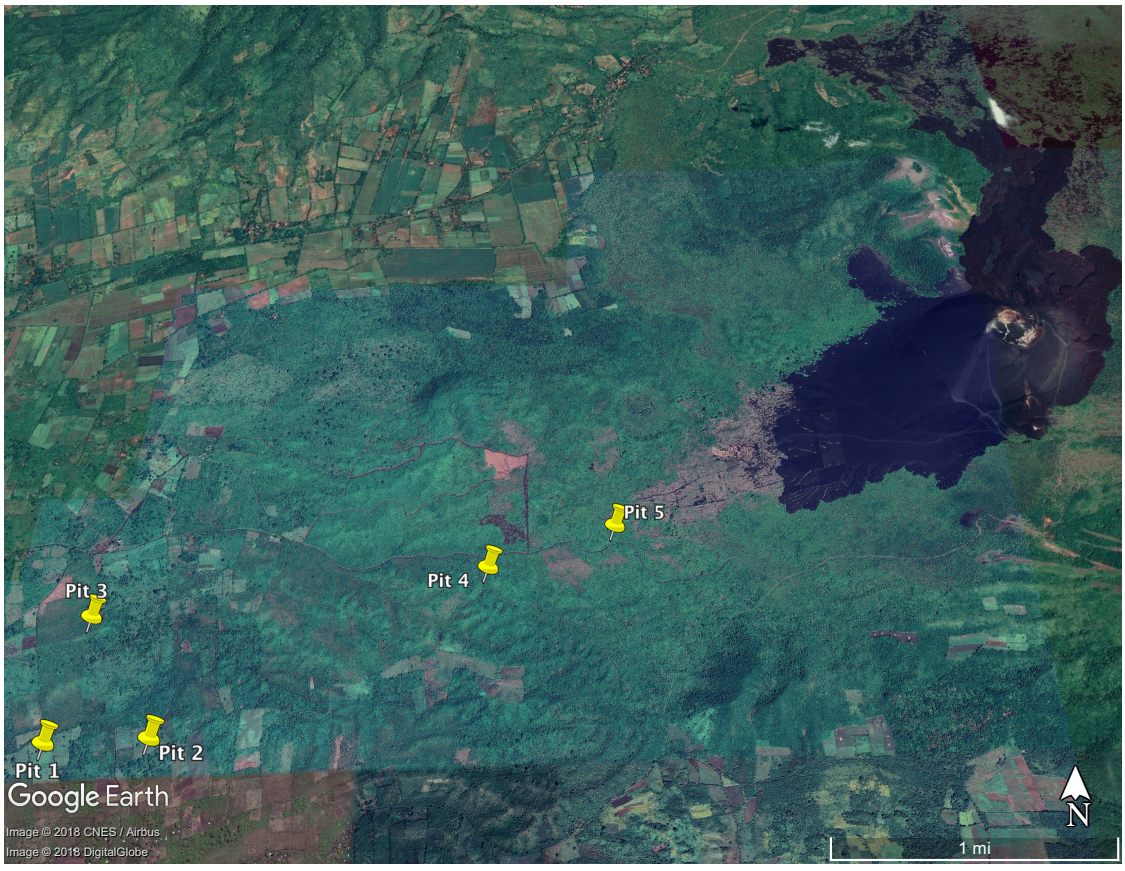

Figure 10 - Google Earth image displaying locations of the pits listed in Table 1 below.

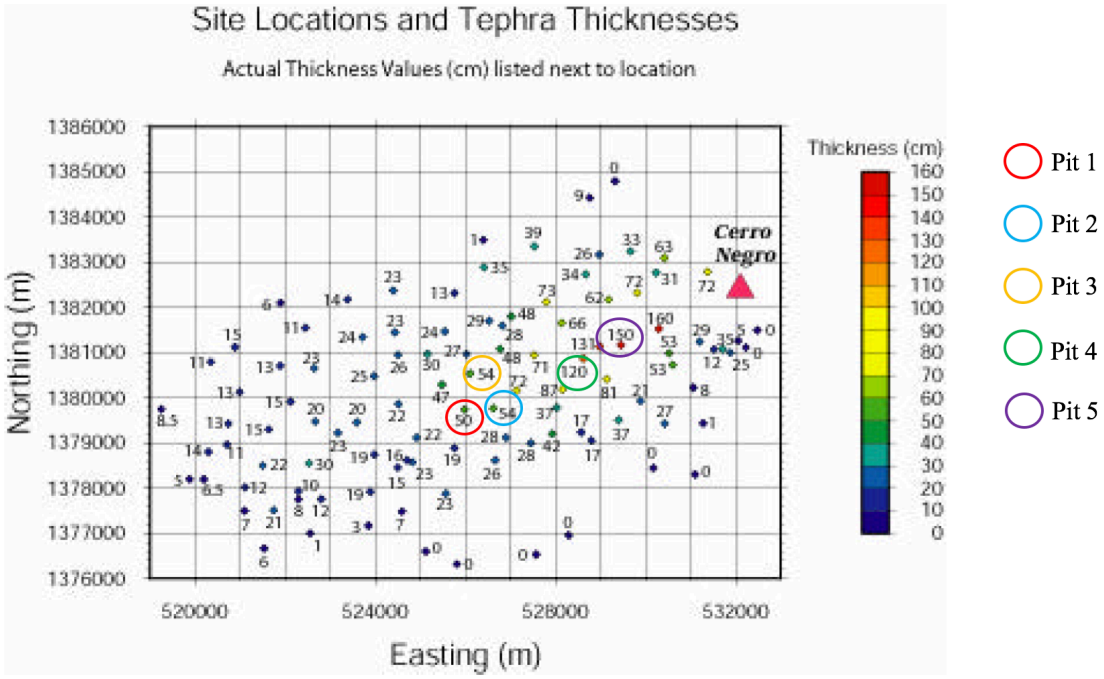

Figure 11 - Pits and tephra thicknesses of the 1992 Cerro Negro eruption from Martin (2004). Circles indicate locations sampled in this study listed in Table 1.

Pit	Northing	Easting	Latitude	Longitude	Thickness
1	1379744	525983	12.480906 N	86.760884 W	50 cm
2	1379772	526617	12.481154 N	86.755049 W	54 cm
3	1380543	526109	12.488131 N	86.759718 W	54 cm
4	1380874	528622	12.491102 N	86.736588 W	140 cm
5	1381172	529451	12.493789 N	86.728956 W	150 cm

Table 1 - Locations and thicknesses of pits of the 1992 Cerro Negro eruption for ash collection shown in Figure 11.

Ash collection from pits 1-4 were conducted on June 1, 2017 and pit 5 on June 2, 2017 with the base of the 1992 eruption determined by depths listed in Table 1 (Martin, 2004) and observation of the coarse, red lithic and soil layer at the 1971/1992 boundary. One-gallon bag samples were collected from pits 1-3 at the base of the pit to 10 cm above, from 10-30 cm, and from 30 cm to the top of the pit. Two one-gallon bag samples were taken from the base of the pit and from 0-10 cm for pit 4 followed by one-gallon bag samples every 20 cm to the top of the pit. Two one-gallon bag samples were taken

from the base of the pit and from 0-20 cm for pit 5 followed by one-gallon bag samples every 20 cm to the top of the pit. All samples are located at the Volatiles Laboratory at the University of New Mexico.

Fumarole gases were collected following the procedure of Giggenbach and Gouguel (1989) in one 100 ml Giggenbach sampling bottle containing approximately 30 ml 5N NaOH and two 200 ml Giggenbach sampling bottles containing approximately 40 ml 5N NaOH on June 3, 2017. One strongly degassing fumarole was sampled (12.506959 N, 86.726389 W) shown in Figure 12 expelling large amounts of steam accompanied by a strong sulfur odor. Gas samples were collected by inserting metal tubes into the fumarole and attaching a rubber hose to each bottle as described in Giggenbach and Goguel (1989). The stopcocks were slowly opened and gas was allowed to flow into each bottle until percolation in the NaOH had ceased after approximately five minutes. Upon completion of gas collection, the temperature of the fumarole was measured and recorded at 148.9 ^{o}C.

Figure 12 - Google Earth image of the fumarole location at Cerro Negro (left). View of the degassing fumarole on June 3, 2017 (right).

3.2 Ash Sample Processing

Approximately one cup of ash was taken from every other one-gallon bag (4-1, 4-3, 4-5, etc.), washed three times in deionized water, placed in a sonic bath for five minutes, rinsed three additional times with deionized water, and left overnight to dry. All samples were sieved into samples that were greater than 500 μm and less than 500 μm. Olivine crystals were handpicked from the greater than 500 μm sample using a binocular microscope. Larger olivine crystals (1-2 mm) with minimal ash cover were chosen and submerged in immersion oil (Cargille Type A, 1.5150 refractive index) and viewed using a petrographic microscope under reflective light to determine which crystals contained melt inclusions. Olivine containing melt inclusions ranging from 30 to 100 μm in diameter with accompanying vapor bubbles were selected for FTIR analysis. The melt inclusions chosen listed with their identification number and location at depth in the tephra column are listed in Table 2.

Melt Inclusion	Depth (cm)
4-1	140
4-3	120 - 100
4-5	80 - 60
4-7	40 - 20
4-8	20 - 0
5-1	150
5-3	130 - 110
5-5	70 - 50
5-7	30 - 10
5-8	10 - 0

Table 2 - Melt inclusion sample numbers and representative depths in the tephra column.

Analysis of these basaltic melt inclusions should show pressures in excess of 3 kbar, compared to basaltic andesite (Roggensack, 2001) or any other more evolved melt

inclusion. Based on the ash chemical composition at Cerro Negro, it should be expected that pressures determined will exceed 3 kbar.

3.3 Ash Chemical Composition

Analysis of ash collected was not performed in this study, however, thorough petrologic analysis of ash from the 1992 eruption was done by McKnight (1995) and this will be discussed here. McKnight noted in his 1995 thesis that phenocrysts of plagioclase, augite, and olivine varying in lengths from 1 to 5 mm were the dominant phases in all the samples and this is what was observed in samples analyzed in this study. Similar to McKnight's samples, olivine is easily found in the ash as both small (1 to 3 mm) whole, euhedral phenocrysts and large, broken phenocrysts, though not all contained melt inclusions. Glass inclusions present were ellipsoidal in shape ranging on the long axis from ~30 to ~150 μm and all glass inclusions analyzed had a vapor bubble present. One inclusion (4-3) contained a plagioclase crystal as was evidenced by its accidental analysis during FTIR sampling and confirmation by microprobe analysis, however, the remaining inclusions showed no other plagioclase inclusions.

Microprobe analysis were performed on both the olivine host crystal and the melt inclusion and the results of those are shown below in Tables 7 and 8 and Figure 17.

3.4 Single-sided Polished Thin Section Preparation

Chosen olivine crystals were mounted to round glass slides using crystal bond epoxy. Each sample was polished on one side for FTIR micro-reflectance and microprobe analysis starting with 15 μm sandpaper to achieve a flat surface and continually polished incrementally down to 0.5 μm sandpaper until the melt inclusion was exposed and any residual scratches removed. It should be noted that as each melt

inclusion was exposed, any intersection with the accompanying vapor bubble results in volatile loss of the vapor bubble.

3.5 FTIR Analysis

FTIR reflectance was performed at the USGS Volcano Science Center in Menlo Park, California using a Nicolet iN10 MX FTIR with an attached liquid-N_2-cooled MCT-B detector. Three spots on each inclusion were analyzed at 16 scans per inclusion to produce a reflectance spectra similar to the procedure of King and Larsen (2013). Melt inclusions 4-1 and 5-3 were large enough to be rotated 180^o and analyzed again to improve data quality and reduce error resulting from non-flat surfaces. Melt inclusion 5-8 had no visible spectra initially, but produced viable spectra upon 180^o rotation and is listed as such in Appendix A. Smoothing of spectra was done using the Omnic Version 8.2 software utilizing 19 smoothing points to reduce noise and then converted to absorbance spectra to allow measuring of peak heights. Baselines were applied to the asymmetric spectra though the use of French curves in OriginPro 2018 given that linear baselines would produce values below the actual concentrations. Average concentrations for water and carbon dioxide listed in Table 3 in the results section were calculated following the equations of King and Larsen (2013), where water is determined by 125*(3650 cm^{-1} peak) and carbon dioxide by 37.2*(2350 cm^{-1} peak) (Figure 13). The relative standard deviation is high given only 3 analyses were performed on each inclusion, however additional analyses would not have improved the results due to the small size of some inclusions and the possibility of non-flat surfaces causing variances in spectra peak heights. Raw data for the peak measurements and volatile concentrations are listed in Appendix A. The coefficients for water and carbon dioxide concentration

calculations were determined by calibration slopes outlined in King and Larsen (2013) shown in Figure 14. Melt inclusion 4-3 had to be discounted when it was discovered on the microprobe that a plagioclase inclusion was analyzed opposed to a glass melt inclusion. Calculation verification of the above technique were performed on two USGS samples of known water and carbon dioxide concentrations determined from attenuated total reflectance. Calculations were within the accepted range of error listed in Lowenstern and Pitcher (2013).

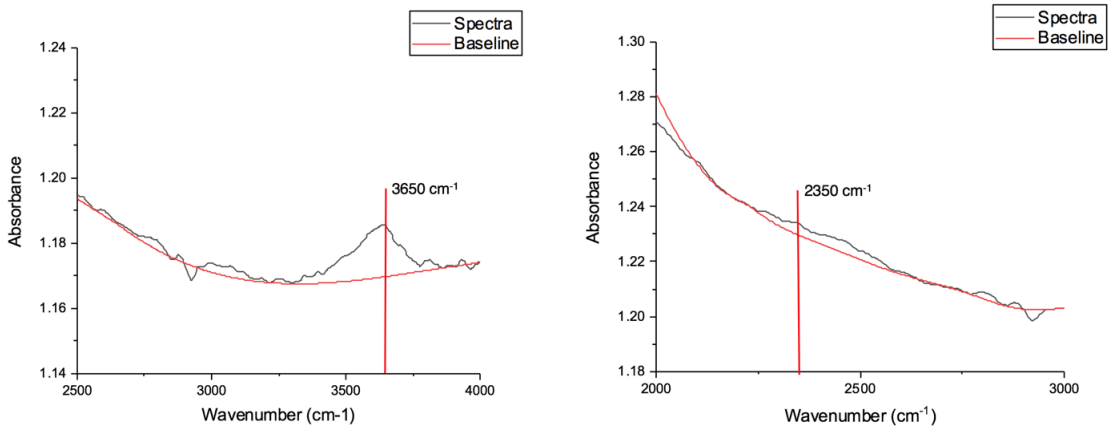

Figure 13 - Representative absorbance peaks used for the calculation of water content (left) and carbon dioxide (right).

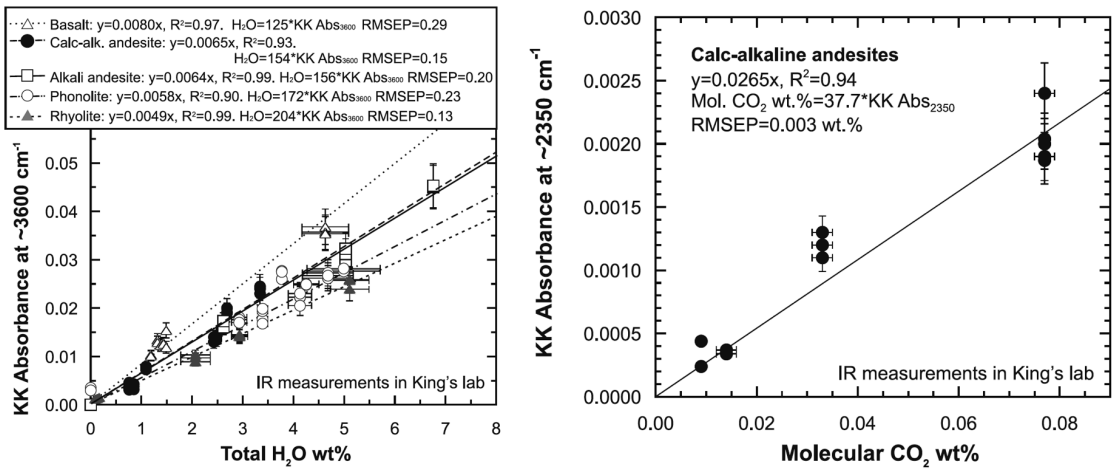

Figure 14 - Calibration curves from King and Larsen (2013) on single-sided FTIR micro-reflectance based on spectra peaks at ~3650 cm^{-1} for H_2O and ~ 2350 cm^{-1} for CO_2.

Spectra listed in the results section show a distinct peak for water around the 3650 cm^{-1}, however, the peak near 2350 cm^{-1} is not as distinguishable, therefore, some assumptions were made as to the peak height closest to the 2350 cm^{-1} wavenumber.

3.6 Vapor Bubble Concentration Calculation

All melt inclusion samples contained vapor bubbles of varying volumes and given the small concentrations of carbon dioxide in the melt inclusions calculated from FTIR analysis, it is likely that a large percentage of the carbon dioxide content is contained in the vapor bubble. Therefore, it is necessary to calculate the carbon dioxide concentration within the bubble and add this back to the amount determined by FTIR of the melt inclusion to get the original carbon dioxide concentration at the time of melt inclusion formation. This is accomplished by determining the volume of the melt inclusion and vapor bubble assuming they have an ellipsoidal shape. The axis normal to viewing was determined by taking the average of the long and short axes, which were measured photomicrographically as shown in Figure 15, following the procedure outlined by Tucker (2018, in review). Tucker determined this method produced the least amount of error when trying to determine the length of the axis normal to viewing. Volume calculations for the melt inclusions and vapor bubbles are shown in Table 4 in the results section.

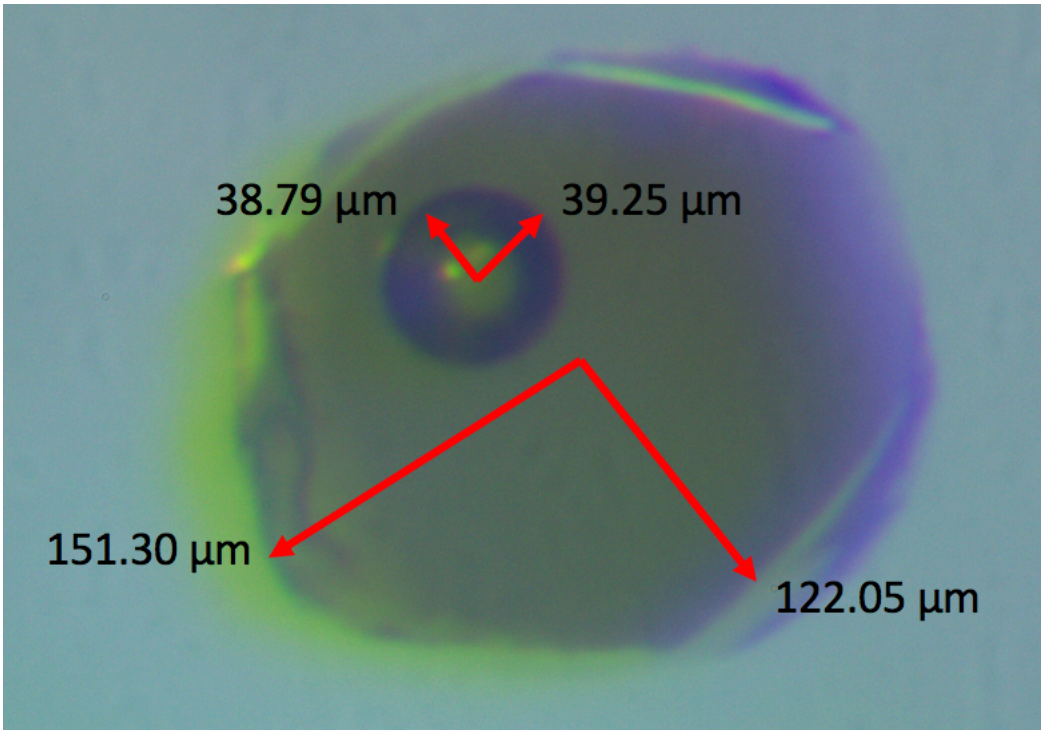

Figure 15 - Photomicrograph of melt inclusion 4-1 that shows the accompanying vapor bubble. Measurements represent the long and short axes used to determine the value of the axis normal to viewing necessary for volume calculations.

Upon calculation of the vapor bubble volume, the Redlich-Kwong equation of state (EOS) was used to determine the molar volume of carbon dioxide within the vapor bubble. Given carbon dioxide's low solubility, it can be assumed that the vapor bubble contents would be pure carbon dioxide (Wallace et al., 2015) and therefore, the molar volume can be used to ascertain the carbon dioxide concentration to be added back to the FTIR calculated concentration. The standard Redlich-Kwong EOS:

$$p = \frac{RT}{V_m - b} - \frac{a}{\sqrt{T}\, V_m \left(V_m + b\right)} \qquad (1)$$

$$a = 0.42748 \frac{R^2 {T_c}^{2.5}}{P_c} \qquad (2)$$

$$b = 0.08664 \frac{RT_c}{P_c} \qquad (3)$$

where the a and b constants are related to the gas being analyzed and can be calculated using the critical temperatures and pressures of that particular gas, in this case, carbon dioxide. For carbon dioxide, the critical temperature is 304.1282 K and the critical pressure is 73.773 bar (Duan & Zhang, 2006). R is the gas constant appropriate for this calculation and T is 1443.15 K based on the trapping temperature from Venugopal et al. (2016). The pressure was calculated using VolatileCalc 2.0 (Newman and Lowenstern, 2002) by determining the saturation pressure based on SiO_2, water and carbon dioxide content along with the trapping temperature. The new average carbon dioxide totals resulting from this calculation are shown in Table 4 in the results section.

3.7 Microprobe Analysis

Microprobe analyses for oxides, sulfur, chlorine, and fluorine were performed using a JEOL JXA-8200 WD/ED combined microanalyzer on eight melt inclusions and ten host olivine crystals at the Microprobe Laboratory in the Institute of Meteoritics at the University of New Mexico under the supervision of Dr. Michael Spilde. Melt inclusion 4-3 was discounted since the inclusion was found to be plagioclase and not glass and 5-3 was not analyzed due to the inability to locate the melt inclusion within the olivine

crystal. Samples were carbon coated and analyzed using a beam current of 25 kV with a beam size of 10 μm. All data is listed in Tables 7 and 8 in the results section.

3.8 Fumarole Gas Analysis

Fumarole gases collected in the head space (dry gas) of Giggenbach bottles were analyzed by gas chromatograph mass spectrometry in the Volatiles Lab at the University of New Mexico under the guidance of Dr. Hyunwoo Lee. The dissolved carbon dioxide within the sodium hydroxide solution (wet gas) was analyzed via titration following the procedures listed in Giggenbach and Goguel (1989). Total sulfur was done by gravimetric analysis as outlined in Giggenbach and Goguel (1989). All results for fumarole gases are listed in Table 9 along with previous measurements done at Cerro Negro for comparison.

4.0 Results

4.1 FTIR

Raw data, spectra, and calculation for each melt inclusion listed in Appendix A.

Sample	H_2O Content	CO_2 Content
4-1	2.56 ± 0.4	65.54 ± 50.1
4-5	1.87 ± 0.2	133.33 ± 40.5
4-7	2.70 ± 0.3	177.54 ± 36.8
4-8	2.20 ± 0.6	201.20 ± 72.7
5-1	2.13 ± 0.4	85.47 ± 43.8
5-3	2.46 ± 0.5	138.88 ± 61.6
5-5	1.82 ± 0.5	75.37 ± 26.0
5-7	1.61 ± 0.3	159.79 ± 45.9
5-8	3.77 ± 1.5	102.39 ± 25.1

Table 3 - Average water and carbon dioxide contents with standard deviations of each Cerro Negro melt inclusion sampled based off FTIR analyses and calculations methods of King and Larsen (2013). Sample 4-3 not listed due to accidental FTIR analysis of a plagioclase inclusion.

Vapor Bubble Volume and Restored CO_2 concentrations

Sample	Pressure (bar)	Bubble Volume %	CO_2 from Spectra (ppm)	CO_2 from Redlich-Kwong (ppm)	Total CO_2 (ppm)	% CO_2 in bubble
4-1	0.794	2.35	65.54	3491	3557	98.16
4-5	0.545	1.34	133.33	2423	2556	94.78
4-7	0.997	0.92	177.54	9926	10104	98.24
4-8	0.750	3.25	119.99	1518	1638	92.67
5-1	0.645	2.41	85.47	1639	1724	95.04
5-3	0.887	2.68	142.39	1621	1763	91.93
5-5	0.499	2.37	75.37	1154	1229	93.87
5-7	0.547	1.42	89.61	1345	1435	93.75
5-8	1.564	1.94	102.39	11313	11415	99.10

Table 4 - Restorative values of CO_2 for each Cerro Negro melt inclusion except 4-3 due to incorrect FTIR analysis. Trapping temperature for each inclusion of 1170 ^{o}C based on Venugopal et al. (2016).

Sample	CO_2 from Spectra (ppm)	Pressure (kbar)	Depth (km)	Restored CO_2 (ppm)	Pressure CO_2 restored (kbar)	New Depth (km)
4-1	65.54	0.794	2.94	3557	6.21	22.97
4-5	133.33	0.545	2.02	2556	3.20	11.83
4-7	177.54	0.997	3.69	10104	8.02	29.67
4-8	119.99	0.750	2.78	1638	2.17	8.03
5-1	85.47	0.645	2.39	1724	3.74	13.84
5-3	142.39	0.887	3.28	1760	4.15	15.36
5-5	75.37	0.499	1.85	1229	2.78	10.29
5-7	89.61	0.547	2.02	1435	2.68	9.90
5-8	102.39	1.564	5.79	11415	11.25	41.63

Table 5 - Depth calculated (3.7 km/kbar) from the average CO_2 values of the sampled Cerro Negro melt inclusions based on FTIR calculations and after restoring original CO_2 values using the Redlich-Kwong equation.

Sample	New depth based on average H_2O and CO_2 ppm (km)	Depth based on minimum H_2O and CO_2 ppm (km)	Depth based on maximum H_2O and CO_2 ppm (km)
4-1	22.97	0.00	25.54
4-5	11.83	10.39	13.49
4-7	29.67	24.57	30.27
4-8	8.03	4.21	12.56
5-1	13.84	4.84	17.79
5-3	14.61	10.53	20.19
5-5	10.29	2.25	16.14
5-7	9.90	3.60	13.46
5-8	41.63	11.11	44.07

Table 6 - New depths of origination for the 1992 Cerro Negro eruption calculated from restored CO_2 concentrations along with the minimum and maximum depths based off minimum and maximum H_2O and CO_2 concentrations from FTIR analysis that were used to calculate additional restored CO_2 concentrations for each sample.

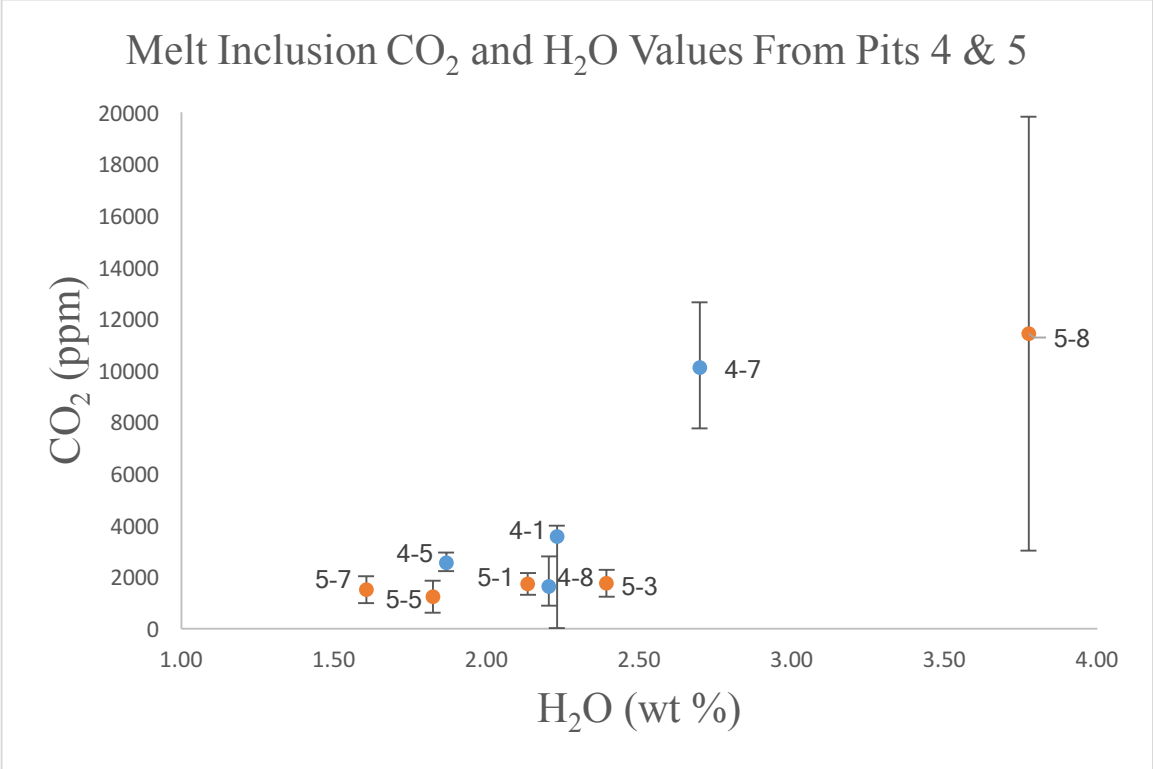

Figure 16 - Plot of CO_2 vs H_2O for each Cerro Negro melt inclusion with CO_2 values restored with error after vapor bubble volume calculation as done by Tucker (2018, in review) and molar volume determination utilizing the Redlich-Kwong equation as done by Wallace et al. (2015). Each melt inclusion is labeled to show variations based on pit depth location (4-1 bottom of pit, 4-8 top of pit).

4.2 Microprobe Analysis

Raw data for each melt inclusion analysis included in Appendix B.

	4-1	4-3	4-5	4-7	4-8
SiO2	48.84	46.83	47.27	46.54	46.30
TiO2	0.92	0.88	1.06	0.78	0.83
Al2O3	17.52	19.38	18.57	16.42	17.86
FeO	9.41	10.01	9.95	11.65	10.22
MnO	0.17	0.19	0.20	0.22	0.18
MgO	5.79	3.99	3.78	5.96	5.14
CaO	10.81	12.33	10.24	10.88	11.99
Na2O	0.43	0.71	0.30	0.48	0.53
K2O	0.37	0.29	0.33	0.24	0.28
P2O5	0.15	0.07	0.19	0.12	0.11
S ppm	1232	1050	1543	720	938
Cl ppm	541	652	521	474	428
F ppm	25	21	24	4	4

	5-1	5-5	5-7	5-8
SiO2	49.00	49.18	48.45	48.39
TiO2	1.12	1.01	0.84	0.88
Al2O3	15.96	16.52	18.09	18.78
FeO	12.09	12.19	9.93	9.05
MnO	0.24	0.22	0.18	0.16
MgO	5.25	5.73	5.34	4.90
CaO	9.82	9.67	11.60	11.42
Na2O	0.51	0.47	0.35	0.40
K2O	0.52	0.34	0.29	0.31
P2O5	0.12	0.10	0.10	0.18
S ppm	540	1154	834	948
Cl ppm	654	502	538	378
F ppm	0	21	13	63

Table 7 - Average oxide, sulfur, chlorine, and fluorine concentrations for each Cerro Negro melt inclusion analyzed. Sample 5-3 omitted due to inability to locate the inclusion on the microprobe.

Raw data for each olivine analyzed included in Appendix B.

	4-1 olivine	4-3 olivine	4-5 olivine	4-7 olivine	4-8 olivine
SiO_2	39.15	38.45	38.84	37.26	38.28
TiO_2	0.00	0.00	0.01	0.01	0.00
Al_2O_3	0.07	0.03	0.03	0.02	0.03
FeO	17.80	18.97	20.25	21.66	19.27
MnO	0.27	0.29	0.34	0.34	0.28
MgO	42.02	40.30	40.03	40.18	40.66
CaO	0.18	0.19	0.17	0.18	0.19
Na_2O	0.00	0.00	0.00	0.01	0.00
K_2O	0.00	0.00	0.00	0.01	0.00
P_2O_5	0.00	0.01	0.02	0.01	0.01
S ppm	26	15	13	51	0
Cl ppm	11	11	50	51	45
FO mol %	80.35	78.64	77.47	76.33	78.52

	5-1 olivine	5-3 olivine	5-5 olivine	5-7 olivine	5-8 olivine
SiO_2	37.68	35.77	38.81	39.58	40.12
TiO_2	0.01	0.01	0.01	0.00	0.01
Al_2O_3	0.03	0.06	0.04	0.11	0.04
FeO	23.76	22.64	22.57	17.93	17.81
MnO	0.41	0.36	0.37	0.30	0.26
MgO	38.24	36.84	38.38	42.27	40.06
CaO	0.21	0.18	0.17	0.19	0.17
Na_2O	0.00	0.01	0.00	0.00	0.00
K_2O	0.00	0.00	0.00	0.00	0.00
P_2O_5	0.01	0.01	0.00	0.01	0.01
S ppm	31	27	5	4	0
Cl ppm	9	28	5	69	28
FO mol %	73.64	73.92	74.77	80.30	79.59

Table 8 - Average oxide, sulfur, chlorine, and FO mol % concentrations for each Cerro Negro host olivine analyzed.

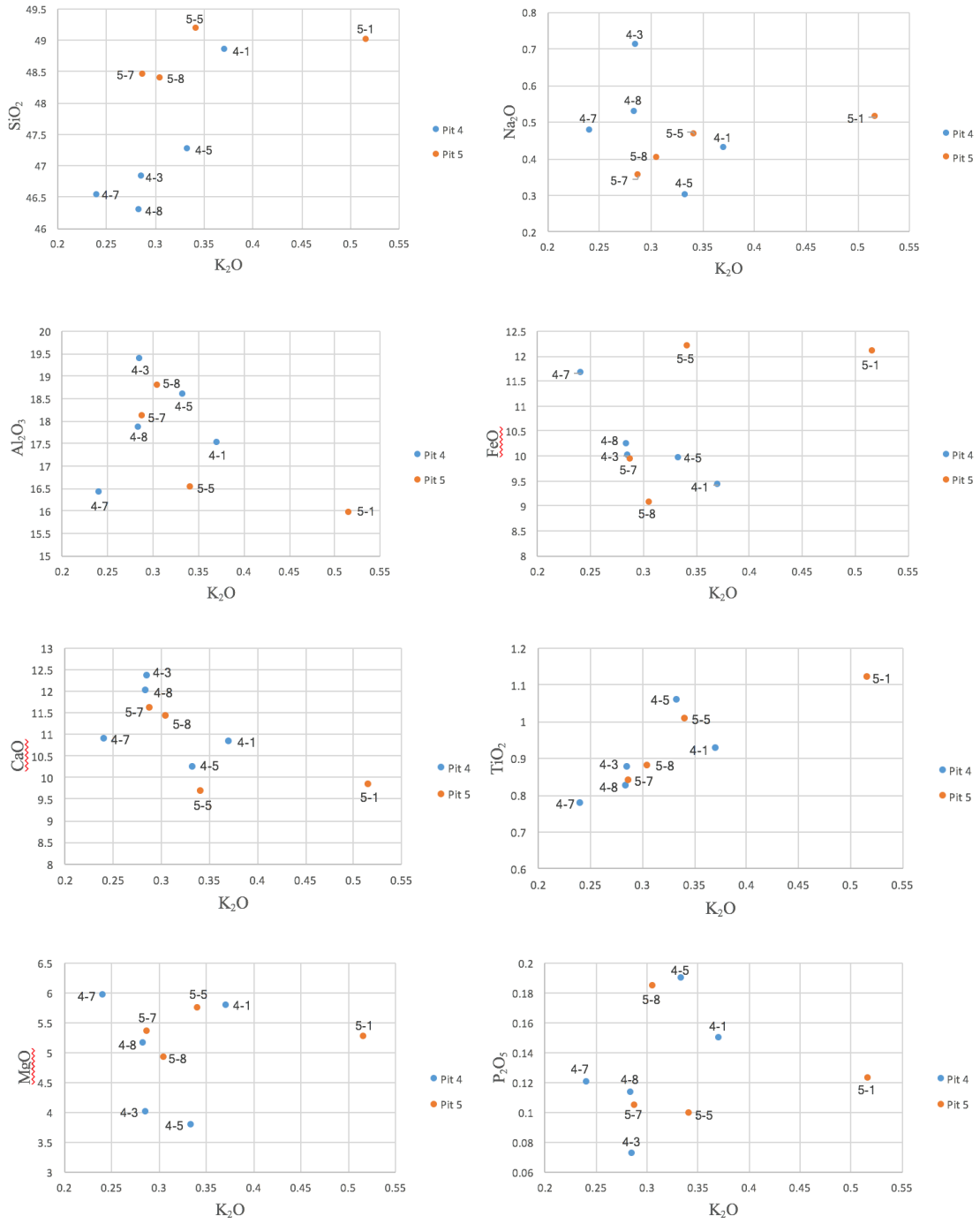

Figure 17 - Major elements vs. K_2O for each Cerro Negro melt inclusion analyzed by microprobe. Though some volatile evolutionary trends can be seen (TiO_2 vs. K_2O), the variability of the inclusions are clear.

4.3 Fumarole Data

	Date	T (°C)	H_2O	CO_2
CN Fumarole	1/16/02	98	922.60	57.43
NIC 14-1 Fumarole	3/15/14	165	957.67	31.90
NIC 14-3 Fumarole	3/15/14	165	966.24	29.99
CN 17-1 Fumarole	6/3/17	149	924.53	66.24
CN 17-2 Fumarole	6/3/17	149	943.18	47.79
CN 17-3 Fumarole	6/3/17	149	963.12	29.33

	SO_2	H_2S	S_t	H_2S/SO_2	C/S Ratio
CN Fumarole			3.37		17
NIC 14-1 Fumarole	0.171	0.057	0.23	0.332	140
NIC 14-3 Fumarole	0.157	0.159	0.32	1.012	95
CN 17-1 Fumarole	2.778	0.000	2.94	0.000	23
CN 17-2 Fumarole	1.273	0.868	2.06	0.682	23
CN 17-3 Fumarole	2.315	1.076	4.17	0.465	7

Table 9 - Fumarole data compiled over time showing the gas content evolution of the existing fumarole at Cerro Negro. Concentrations in mmol/mol.

	CO_2 ppm (Restored)	S ppm	C/S Ratio	Cl/F Ratio
4-1	3557	1232	2.9	22
4-5	2556	1543	1.7	22
4-7	10104	720	14.0	119
4-8	1638	938	1.7	105
5-1	1724	540	3.2	0
5-5	1229	1154	1.1	24
5-7	1505	834	1.8	43
5-8	11415	948	12.0	6

Table 10 - C/S ratios calculated from microprobe data and average restored CO_2 values for sampled Cerro Negro melt inclusions. Note the much lower values compared to fumarole data. Cl/F ratios for each sample calculated from microprobe data are included.

5.0 Discussion

5.1 H_2S/SO_2 Ratios from Fumaroles

In a study done by Moor et al. (2016) H_2S/SO_2 ratios from fumarole sampling greater than 0.3 are a relatively unambiguous indicator of hydrothermal interaction. Based on the fumarole data listed in Table 9, the H_2S/SO_2 ratio indicates that Cerro Negro exhibits a hydrothermal interaction at depth given that the ratio is greater than 0.3 and has been for at least fifteen years. When comparing Cerro Negro to other arc volcanoes worldwide, it is evident that volcanic systems across these regimes show variations from purely magmatic (<0.3 H_2S/SO_2 ratio) to highly hydrothermal (>0.3 H_2S/SO_2 ratio). Studies done at Etna (Roberts et al., 2017) and Redoubt (Werner et al., 2013) display a clear magmatic signature with H_2S/SO_2 ratios of 0.02 and 0.1 respectively. In contrast, analyses done at Lastarria (Lopez et al., 2018), Poas (Fischer et al., 2015) and Vulcano (O'Dwyer et al., 2003) give clear hydrothermal signatures with H_2S/SO_2 ratios of 0.21, 0.6 - 0.4, and 0.7 - 6.3 (Chiodini et al., 1995). The variations seen in the H_2S/SO_2 ratios is a direct result of the fumarole temperature. At temperatures above 445 ^oC, the boiling point of elemental sulfur, significant remobilization to the gas phase will occur that can lower the H_2S/SO_2 ratio. At Etna, Madonia et al. (2013) recorded a fumarole temperature of up to 500 ^oC, high enough to increase the SO_2 content and lower the H_2S/SO_2 ratio. In contrast, at Lastarria, Lopez et al. (2018) recorded a fumarole temperature of 260 ^oC, Fischer et al. (2015) measured a fumarole temperature of <100 ^oC at Poas, and O'Dwyer et al. (2003) noted a fumarole temperature of 271 ^oC at Vulcano, all significantly lower than the boiling point of sulfur allowing for more

interaction with subsurface water increasing the H_2S/SO_2 ratio that gives the hydrothermal interaction signature. Therefore, based on the low temperature of the fumarole, it can be concluded that there is a hydrothermal interaction present at Cerro Negro and the presence of this hydrothermal interaction can have a large effect on carbon/sulfur ratios expressed in fumarole gases sampled at the surface.

5.2 Carbon/Sulfur Ratios - Fumarole vs. Melt Inclusion Analysis

CO_2/S_T ratios are an additional indicator of magmatic vs. hydrothermal interaction where ratios greater than 4.5 could indicate pulses of deeply derived CO_2-rich gas preceding explosive activity (Moor et al., 2016). The $CO_2/S_{total,}$ CO_2/SO_2, or C/S ratio is commonly used to assess variations in volcanic activity because the solubility of CO_2 and S in magmas differ significantly (Carroll and Webster, 1994; Holloway and Blank, 1994) and upon magma ascent CO_2 is expected to degas first, resulting in high C/S ratios. For instance, Aiuppa et al. (2005) showed that an increase in C/S ratio potentially indicates renewed magmatic activity at Vulcano, and that an increase in C/S ratio in combination with an increase in CO_2 flux is a strong indicator of renewed volcanic activity likely due to the injection and degassing of new magma into the system at Stromboli (Aiuppa et al., 2009).

Aiuppa et al. (2014) looked at several volcanoes around the world as well as along the Central American Volcanic Arc (Figure 18), and upon closer investigation of the volcanoes in Nicaragua, they discovered that trends converge at high temperature fumaroles (>455 ^oC) to CO_2/S_T ratios of ~3 in Nicaragua. From the data in Table 9, the fumarole at Cerro Negro shows C/S ratios up to two orders of magnitude larger than the average value shown by Aiuppa et al. (2014). The cause of this in the case of Cerro

Negro is due to the low-temperature (148.9 ^{o}C) fumarole that is not representative of magmatic gas. This occurs due to their deep CO_2/S_T magmatic fingerprint being obscured by selective scrubbing of water-soluble S (Symonds et al., 2001): this is reflected by the high CO_2/S_T ratios (up to >1000) in some of the low-temperature crater gas manifestations (Aiuppa et al., 2014). Therefore, due to the hydrothermal interaction and low-temperature of the fumarole at Cerro Negro, CO_2/S_T ratios are controlled by sulfur partitioning into the liquid hydrothermal system or gas scrubbing reactions in a shallow subsurface environment (Symonds et al., 2001), and as such cannot be used to track volatile origin at depth (Aiuppa et al., 2017). Therefore, this study will focus on C/S ratios from melt inclusions that should be more representative of magmatic gas compared to the hydrothermal signature seen at the low-temperature fumarole measurements.

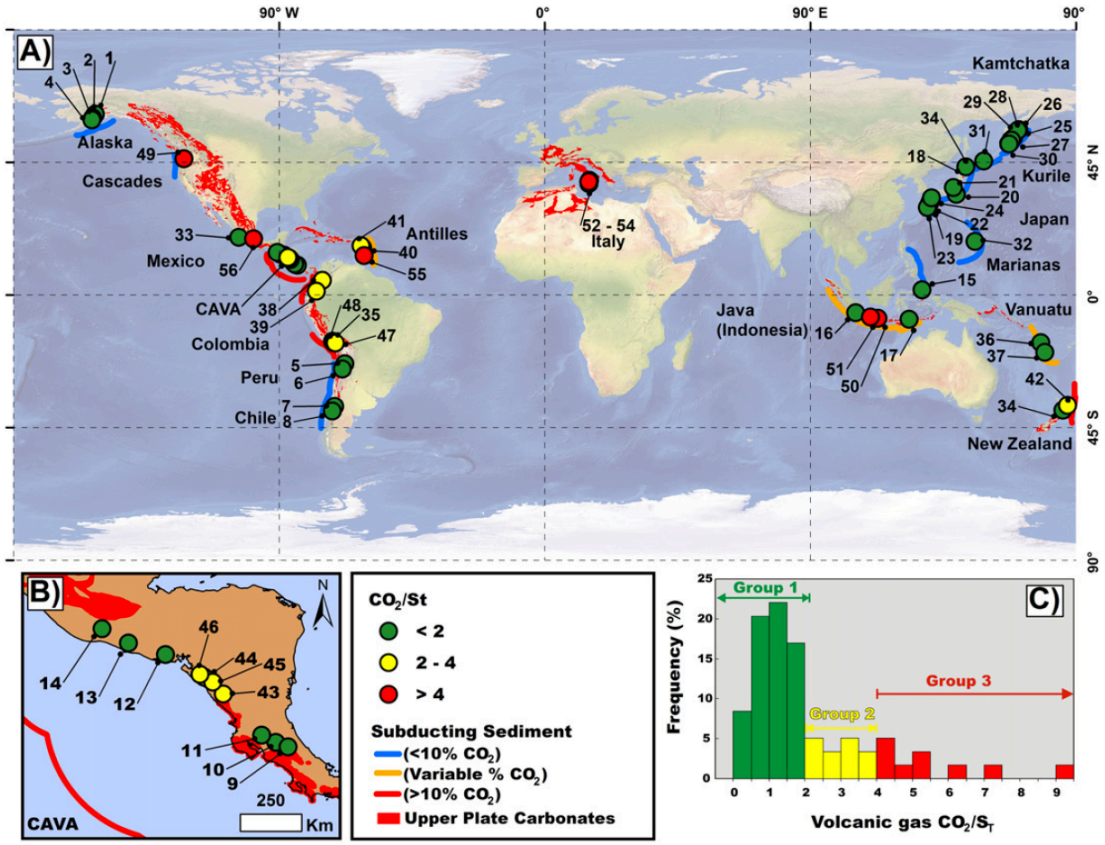

Figure 18 - C/S ratios from volcanic arc systems around the world with the inset (B) narrowing in on volcanoes in Nicaragua displaying a C/S ratio in the range of 2 - 4 from Aiuppa et al. (2017). The ratios are based on high-temperature fumaroles, however this study will utilize C/S ratios from melt inclusions due to the nature of the low-temperature fumarole sampled at Cerro Negro.

Given the low-temperature nature of the fumarole gas at Cerro Negro, it is clearly not magmatic, however, magmatic (+mixed) gases, instead, are characterized by means of magmatic arc gas CO_2/S_T ratios of ~2.5 (Aiuppa et al, 2017). From the data presented in Table 10, the mean C/S ratio of melt inclusions analyzed is 4.8, somewhat higher to the mean determined for arc volcanoes shown in Figure 18 from Aiuppa et al. (2017) due to elevated CO_2 contribution from the eruption. Therefore, melt inclusions give a better picture of the volatile concentration and state of the magma at depth, however it is interesting to note that the melt inclusions analyzed in this study are variable throughout

the tephra column, which will be discussed in the next section. As new inputs of magma are introduced into the volcanic system, the CO_2/S_T ratio increases substantially as new pulses of CO_2-rich magma ascend from depth. The fumarole CO_2/S_T ratios above suggest that this undegassed magma sits very close to the surface, which as seen by the low temperature of the fumarole as well as the lack of a presence of a lava lake proves otherwise. Therefore, melt inclusion analysis is the most reliable source in order to determine volatile concentrations at depth in low temperature fumarole systems, which encompass a large quantity of volcanic systems worldwide. All previous results for C/S ratios at arc volcanoes have been done by analysis of either the fumarole or the degassing plume. This study adds a new technique to the analysis toolbox where melt inclusions that tend to be easier to sample than vent gases, can be used to determine background C/S levels.

One key factor in this analysis is that the CO_2/S_T ratios calculated would not be robust if the CO_2 concentration lost to the vapor bubble is not added back to the total CO_2 content. If only the CO_2 concentration from the FTIR analysis on the melt inclusion is used without considering the vapor bubble, the CO_2/S_T ratios would be up to two orders of magnitude less, not representative of the magma at depth that melt inclusions sample. Consequently, future analysis where melt inclusion data is utilized must include the volatile content in the vapor bubble to be robust.

5.3 Cl/F Ratios

Another ratio that can be looked at to determine level of degassing is the Cl/F ratio, where low ratios (~16) show a high level of degassing (Taran et al., 2018). This is due to the high solubility of fluorine in silicate melts, thus if the magma is highly

degassed, the fluorine content increases and therefore lowers the Cl/F ratio. The way this ratio can be applied in this study is by looking at sample 5-8, the melt inclusion with the largest CO_2 content after CO_2 restoration. The Cl/F ratio is 6, meaning a high level of degassing, however, this is for the melt inclusion. This can be interpreted that the melt inclusion is highly degassed and that the volatile loss is contained within the vapor bubble leading to the large CO_2 concentration determined when calculating the restorative value. Though this could be an additional check on degassing trends, this is not without trepidation. The Cl/F ratio for the next highest volatile melt inclusion (4-7) is 119 meaning the melt inclusion is not as degassed, however, the volatile content calculated in the vapor bubble is 98%, similar to the 99% of sample 5-8 that is highly degassed based on the Cl/F ratio. Consequently, using the Cl/F ratio can be useful, however, knowledge of the true amount of degassing is still highly variable and uncertain.

5.4 Reasons for Variability - Disequilibrium in the Magma Holding Body

Ideally, in introductory geology textbooks, we would picture the magma holding body in equilibrium and upon eruption, tephra recovered would represent the magma concentration from top to bottom as the magma holding body is evacuated. Based on the data in this study, this inference is not accurate given that the volatile concentrations are variable throughout the ash column represented by the melt inclusion analyses. If equilibrium was present, expectations suggest that the melt inclusions at the bottom of the pit (4-1 and 5-1) would contain the highest volatile concentrations, however, as seen in Figure 16 this is not the case. Therefore, and not surprisingly, it cannot be assumed that there is simply a large magma body that erupts from top to bottom in one continuous

event. The melt inclusion data suggests that formation could be at any depth and the dynamics of the magma holding body transport melt from below where it can possibly be stalled at a shallower depth prior to eruption lending to the variability of volatile content throughout the tephra column.

5.5 Reasons for Variability - Magma Input During Eruption

Building on the previous section, an ideal eruption starts when volatile content exceeds the holding capacity resulting in an eruption that drains the entire magma body in one event, however, as observed from countless occurrences, eruptions ebb and flow due to new inputs of magma during the evacuation process. With new inputs of magma, the volatile content would also be variable throughout the tephra column that show periods of magma recharge and quiescence. This process should be tracked by the CO_2/S_T ratio in the melt inclusions similar to vent degassing that represent variable melt concentrations at depth as the eruption evolves in response to magma concentration. This was shown to be accurate in a study done on the March, 2015 eruption of Villarrica volcano by Aiuppa et al. (2017). During background degassing Phase I (13 November, 2014 to 25 January, 2015), the derived CO_2/SO_2 ratios in the gas discharges were systematically lower than 3 (range 0.65 - 2.7), and mostly between 1 and 2. Starting from January 26, or Phase II (26 January to 5 February), the CO_2/SO_2 ratios fluctuated more widely, and peak values as high as 8.3 were noticed with the mean CO_2/SO_2 ratio of 2.1. Fluctuating high (up to 9.1) CO_2/SO_2 ratios persisted during Phase III that preceded the March 3 eruption with the mean CO_2/SO_2 ratio of 2.7, or the highest of the 3 periods (Aiuppa et al., 2017). The steady increase in CO_2/SO_2 ratios up to the eventual eruption show that spikes in the CO_2/SO_2 ratio can indicate new impulses of magma into the volcanic system. Similarly,

the observations made at Villarrica are reminiscent of the CO_2/SO_2 cycles seen prior to eruption at other volcanoes, such as Etna (Aiuppa et al., 2007, 2010a; Patane et al., 2013), Redoubt (Werner et al., 2013), and Turriabla (de Moor et al., 2016). The data from the Cerro Negro melt inclusions show that this could be an explanation for the 1992 eruption. Variability in melt inclusion contents and CO_2/S_T ratios throughout the tephra column could record how the magma was evacuated from the holding body with possible recharge events from the introduction of new magma. As the CO_2/S_T ratio increases, it can be hypothesized that new magma is being added. The data from pits 4 and 5 show a large increase in the CO_2/S_T ratio occurring towards the end of the eruption. Based on the CO_2/S_T ratio, the hypothesis can be made that pulses of new magma were added during the eruption from varying depths until the entire magma body was evacuated.

5.6 Reasons for Variability - New Perspective on the Plumbing System

The previous two sections have suggested that there is a large magma body that is evacuated completely during eruption, however, is this a reasonable schematic of the plumbing system beneath Cerro Negro? It has been hypothesized for the 1992 eruption shown from Venugopal et al. (2016) (Figure 19) that a magma chamber exists beneath Cerro Negro at 8 km with a large magma source near 14 km. Roggensack et al. (1997) states that magma rich in water and carbon dioxide content ascended to a level of 6 km before the large Strombolian eruption in 1992, though not shown in the Venugopal et al. (2016) figure. MacQueen et al. (2016) performed a gravity anomaly analysis at Cerro Negro and determined from the density contrast between basaltic inclusions and volcanic tephra that there are shallow intrusive complexes providing avenues for magma transport. However, the density anomalies imaged in the MacQueen study likely only represent the

shallowest portion of a deeper multi-level magma plumbing system feeding Cerro Negro. An issue with gravity anomaly analysis is that shallow structures (< 2 km) are resolved more precisely than deeper structures meaning that gravity anomaly differences are likely not the best way to resolve magma chambers at larger depth. Additionally, the melt inclusion data from Venugopal et al. (2016) and Roggensack (1997) show great variability similar to my sampled melt inclusions meaning that the inclusions are sampling melt from various depths within the plumbing system that also cannot be resolved by gravity anomaly analysis. Therefore, it is more plausible to deduce that the melt inclusions originated from varying deeper sources that were entrained from these variable locations in the 1992 eruption.

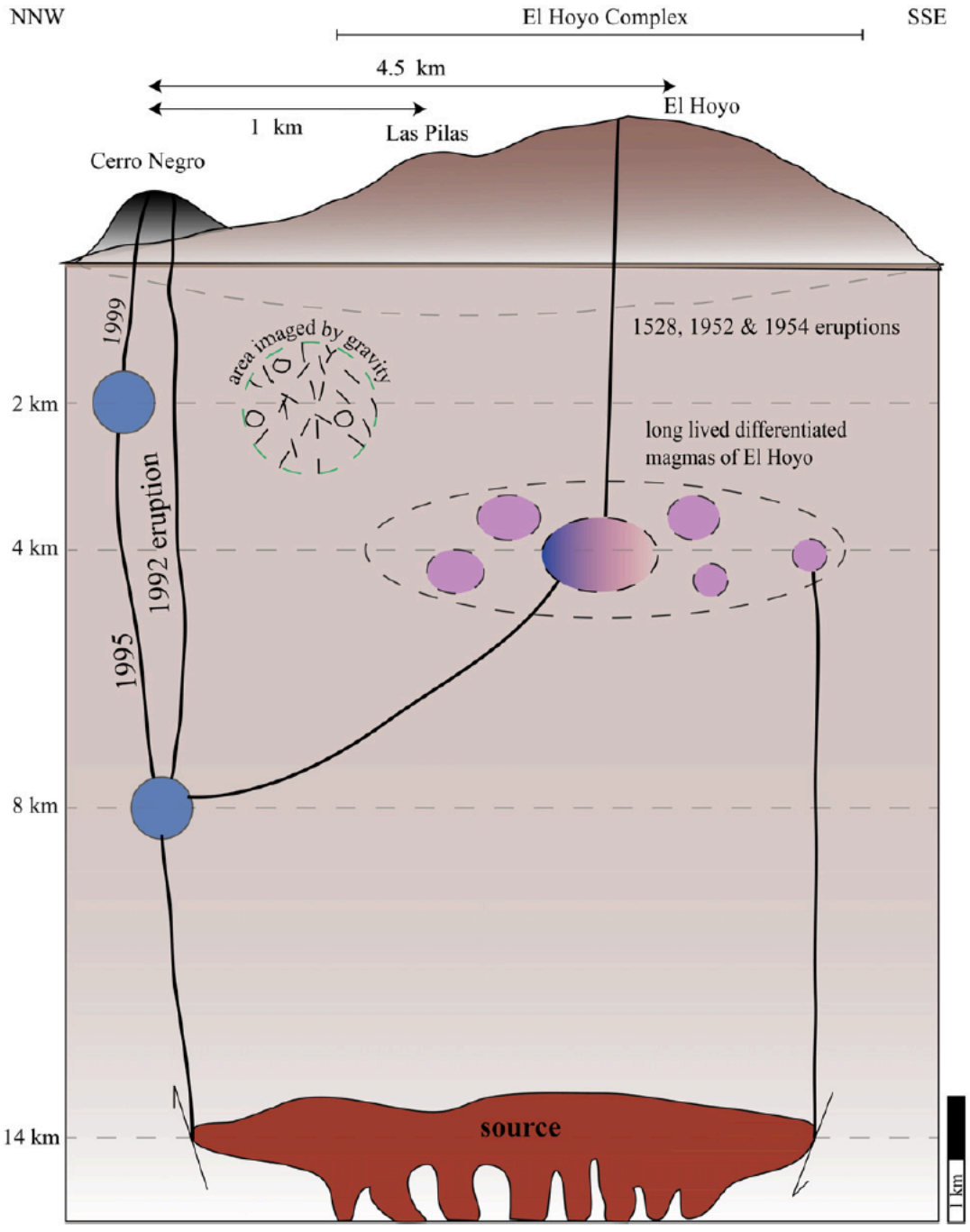

Figure 19 - The proposed model for the plumbing system beneath Cerro Negro and the El Hoyo Complex from Venugopal et al., 2016. This illustration is a combination of previous studies, notably: 14 km primitive source region (Roggensack, 2001), Cerro Negro reservoirs at 7–8 km (Roggensack et al., 1997; MacQueen, 2013).

In contrast to the schematic of Venugopal et al. (2016), the more realistic view of the plumbing system is a series of magma lenses beneath Cerro Negro similar to the diagram in Cashman et al. (2017) (Figure 20). The variation in content of the melt inclusions is better explained from origination of separate magma holding bodies at depth that are in discrete equilibrium compared to a large magma body maintaining overall equilibrium. Though the results of melt inclusion analysis by Venugopal et al. (2016) and Roggensack (1997) suggest a shallow magma holding body, the inability of geophysical methods to identify large melt-rich bodies in the upper crust, by contrast, suggests that large volumes of upper crustal melt are likely ephemeral, therefore, it is more likely that crystals with different histories, stored in different parts of the magmatic system, are transported to the growing upper crustal magma chamber and amalgamated shortly before eruption (Cashman et al., 2017). Therefore, one alternative mechanism is to rapidly redistribute melt from vertically stacked lenses into a single magma chamber (Allan et al., 2013; Christopher et al., 2015; Wotzlaw et al., 2015).

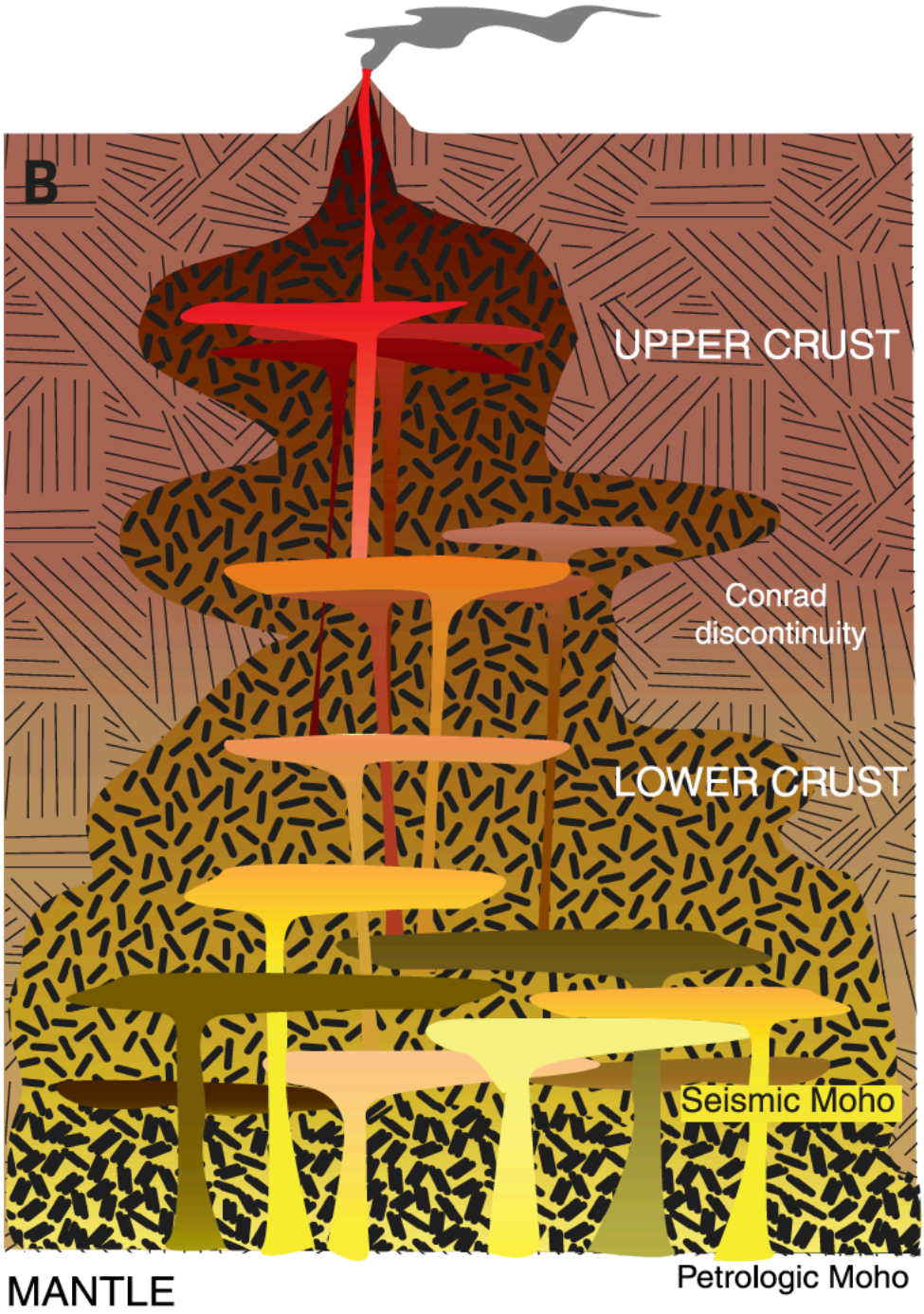

Figure 20 - Transcrustal magmatic system from Cashman et al., 2017, where melt processing in the deep crust produces melts that are transferred to mid- and finally upper crustal levels. The potential for transient vertical connectivity in this system presents the possibility of successive destabilization of melt lenses (Christopher et al., 2015).

What makes this an innovative hypothesis is that this type of magma lens structure has mainly been applied to regions with axial spreading centers. In extensional environments such as mid-ocean ridges, identified melt lenses are thin and sill-like in shape (Kiser et al., 2016; Ward et al., 2014; Hill et al., 2009), where distributed melt lenses can destabilize rapidly to accumulate in the shallow crust, or are tapped syn-eruptively to produce large cumulative erupted volumes (Cashman et al., 2014). However, with the new study done by Cashman et al. (2017), the application of the melt lens hypothesis to transcrustal magmatic systems is gaining ground, and the example of Cerro Negro in Nicaragua proves to be a prime example.

If magma lenses are more likely to be present in extensional regimes, the tectonic setting for Cerro Negro shown in Figure 4 displaying a region of transform faults creating the extensional horst and graben subsurface provides the perfect transcrustal setting for the formation of magma lenses. The variability in the volatile contents shown from melt inclusion analysis suggest that their origination from greatly varying depths is better explained by contributions from several magma holding bodies that are amalgamated into one larger erupting body as the system destabilizes as the eruption proceeds. The schematic from Venugopal et al. (2016) (Figure 19) showing magma holding bodies at 8 km and a source at 14 km for the 1992 eruption is accurate, however, I argue that the magma holding bodies at these depths are lenses part of a larger system shown in Figure 22. The magma lens hypothesis better explains the variability in the melt inclusion volatile concentrations in my analysis. Additionally, the melt inclusion analyses done by Venugopal et al. (2016) and Roggensack (1997) do not account for the carbon dioxide concentration within the vapor bubble and therefore ignore possible magma sources at

greater depth.

A notable difference in the schematic presented in this study are the magma holding bodies at depths an order of magnitude larger than presented in previous analyses. Based on tomographic data collected by the Tomography Under Costa Rica and Nicaragua (TUCAN) seismometers, the depths of originating melt presented in Figure 22 are realistic. Based off low velocities in the subducted plate, more so beneath Nicaragua, suggest hydration of the subducted crust and upper mantle to 150 km depth. A sheet of elevated Vp/Vs, suggesting possible melt, rises from the slab beneath the volcanoes in Nicaragua (Figure 21), supporting the possibility of localized region of melt vertically connecting the slab to the volcanoes (Syracuse et al., 2008), which could provide the magma for each discrete lens beneath the Cerro Negro volcanic complex.

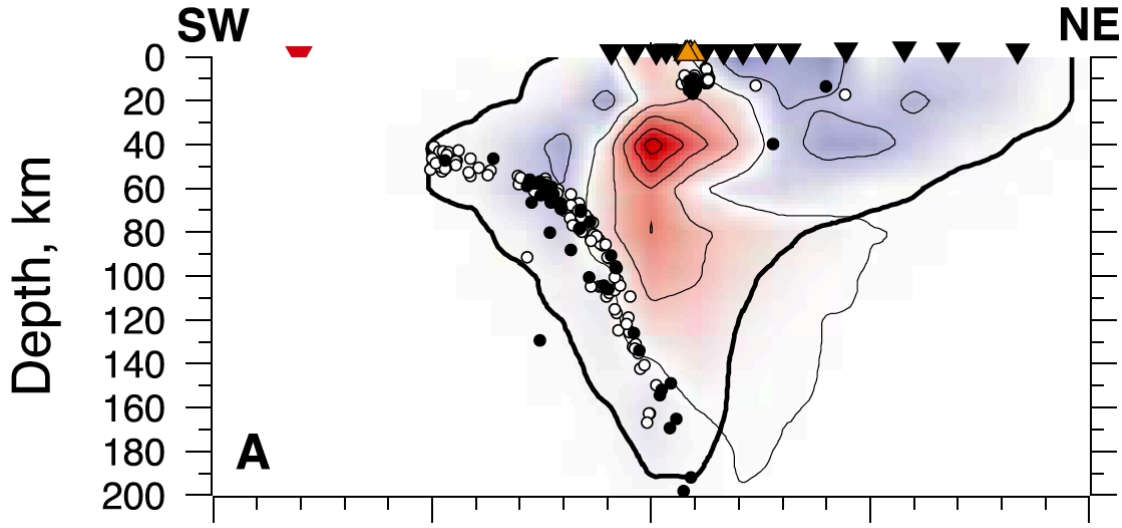

Figure 21 - Tomographic imaging from Syracuse et al. (2008) based of Vp/Vs ratio beneath the volcanoes of Nicaragua, shown as orange triangles at the surface. The black inverted triangles represent TUCAN seismometers used for the analysis. Circles represent hypocenters along the subducting slab that indicate depths of subduction up to 200 km with a vertical Vp/Vs contrast beneath the Nicaraguan volcanoes that suggest melt could emanate from greater depths than previously believed.

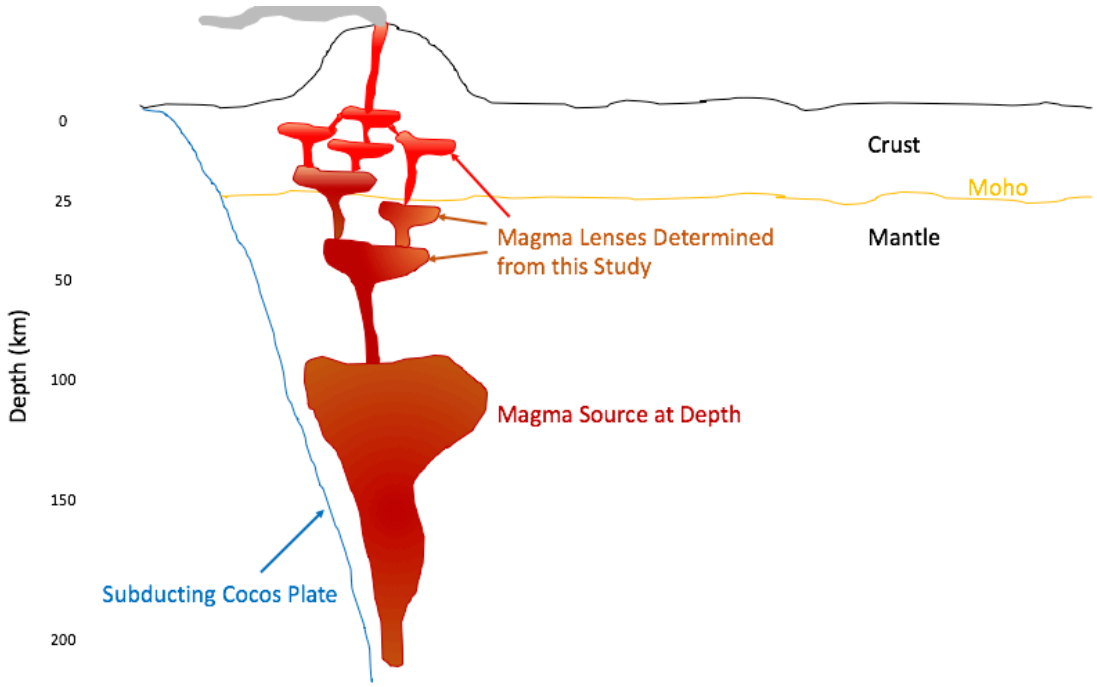

Figure 22 - Proposed schematic of Cerro Negro's plumbing system based off melt inclusion analysis done in this study.

6.0 Conclusion

Though advances have been made in the analysis of plumbing systems at volcanic complexes, more investigation into the dynamic processes are necessary. Melt inclusions act as a tiny pressure vessel allowing melt inclusions to remain at higher pressure than the ambient melt surrounding the crystal as the magma ascends and eventually erupts quenching to glass. Thus, analysis of melt inclusions can potentially provide a record of magmatic conditions, including dissolved volatile components, at the time of crystal growth (Lowenstern, 1995; Danyushevsky et al., 2002; Metrich and Wallace, 2008, Wallace et al., 2015) and give us the best snapshot to the subsurface plumbing architecture.

The ability to quantify water and, in particular, carbon dioxide concentrations at depth through the analysis of melt inclusions is key. The presence of carbon dioxide

within the melt inclusion is an indication of high-pressure entrapment (Wallace, 2005) and will change quickly as the magma ascends and depressurizes relative to water, which stays fairly constant due to its increased solubility in magma. Thus, carbon dioxide is a great indicator of depth of formation based on the pressure calculated from the carbon dioxide concentrations. However, a concern with melt inclusions involves the process during post-entrapment cooling and crystallization where the pressure decrease causes nucleation of a vapor bubble inducing loss of volatiles from the melt into the bubble (Anderson and Brown, 1993, Steele-MacInnis et al., 2011, Moore et al., 2015, Wallace et al., 2015, Aster et al., 2016). Therefore, this study has shown that due to the high percentage of carbon dioxide loss to the vapor bubble, up to 99% in some cases, the content within the vapor bubble must be added back to the original carbon dioxide measurements obtained from FTIR analysis to give a true concentration recorded at depth. This is further supported by the CO_2/S_T ratio calculated in this study that would be understated up to two orders of magnitude without the vapor bubble carbon dioxide contents restored and would not be consistent with the previously recorded CO_2/S_T ratios for the Nicaraguan volcanic front.

The restored carbon dioxide values, newly calculated depths of formation and the CO_2/S_T ratios show a high variability among the tephra erupted during the 1992 eruption. After exploring possible explanations for this variability, the best scenario proposed based on the volatile inconsistency and the tectonic setting results in a new perspective on the plumbing system at Cerro Negro. Previous studies present a schematic of a magma chamber at 8 km depth supplied by a deeper magma source at 14 km, however, the analyses of melt inclusions in studies done by Venugopal et al. (2016) and Roggensack

(1997) are highly variable and do not take into consideration the carbon dioxide content within the vapor bubble. Consequently, based on a new schematic proposed by Cashman et al. (2017), the volatile variability is better explained by the existence of a network of subsurface magma lenses supplying the main conduit at eruption versus the traditional view of long-lived magma chambers at depth that are evacuated at the time of eruption.

Unfortunately, at the present time, speculation on the plumbing system is simply that. Continued investigation through the use of tomographic data need to be acquired to better constrain where melt resides at depth. If the proposed NSF project for volcano communities in Nicaragua comes to fruition, a better understanding of the subsurface environment at several volcanoes in Nicaragua including Cerro Negro can be realized. Employing melt inclusion analysis and tomographic data could provide a system that can be applied to other prevalent volcanic systems around the world that pose a threat to society. Collection of melt inclusions from tephra is less harmful than sampling direct degassing and can provide an overall picture of volcanic eruption evolution over time as well as provide background levels expected at particular volcanic arc systems. Increased knowledge of where magma resides at depth in addition to when this magma is rising is the key factor in determining possible volcanic activity and helping to mitigate damage and loss of human life.

References:

Aiuppa, A, Federico, C., Giudice, G., Gurrieri, S., 2005. Chemical mapping of a fumarolic field: La Fossa Crater, Vulcano Island (Aeolian Islands, Italy). Geophysical Research Letters. 32, 1-4.

Aiuppa, A., Moretti, R., Federico, C., Giudice, G., Gurrieri, S., Liuzzo, M., Papale, P., Shinohara, H., Valenza, M., 2007. Forecasting Etna eruptions by real-time observation of volcanic gas composition. Geology. 35, 1115-1118.

Aiuppa, A., Federico, C., Giudice, G., Giuffrida, G., Guida, R., Gurrieri, S., Liuzzo, M., Moretti, R., Papale, P, 2009. The 2007 eruption of Stromboli volcano: Insights from real-time measurement of the volcanic gas plume CO_2/SO_2 ratio. Journal of Volcanology and Geothermal Research. 182, 221-230.

Aiuppa, A., et al., 2010a. Patterns in the recent 2007-2008 activity of Mount Etna volcano investigated by integrated geophysical and geochemical observations. Geochemistry, Geophysics, Geosystems. 11, 1-13.

Aiuppa, A., Robidoux, P., Tamburello, G., Conde, V., Galle, B., Avard, G., Bagnato, E., de Moor, J.M., Martínez, M., Muñoz, A., 2014. Gas measurements from the Costa Rica-Nicaragua volcanic segment suggest possible along-arc variations in volcanic gas chemistry. Earth and Planetary Science Letters. 407, 134-147.

Aiuppa, A., Bitetto, M., Francofonte, V., Velasquez, G., Parra, C.B., Giudice, G., Liuzzo, M., Moretti, R., Moussallam, Y., Peters, N., Tamburello, G., Valderrama, O.A., Curtis, A., 2017. A CO_2-gas precursor to the March 2015 Villarrica volcano eruption. Geochemistry, Geophysics, Geosystems. 18, 2120-2132.

Allan, A.S.R., Morgan, D.J., Wilson, C.J.N., Millet, M.A., 2013. From mush to eruption in centuries: Assembly of the super-sized Oruanui magma body. Contribution to Mineral Petrology. 166, 143-164.

Anderson, A.T., Brown, G.G., 1993. CO_2 contents and formation pressures of some Kilauean melt inclusions. American Mineralogist. 78, 794-803.

Aster, E.M., Wallace, P.J., Moore, L.R., Watkins, J., Gazel, E., Bodnar, R.J., 2016. Reconstructing CO_2 concentrations in basaltic melt inclusions using Raman analysis of vapor bubbles. Journal of Volcanology and Geothermal Research. 323, 148-162.

Barckhausen, U., Ranero, C.R., von Huene, R., Cande, S.C., Roeser, H.A., 2001. Revised tectonic boundaries in the Cocos Plate off Costa Rica: Implications for the segmentation of the convergent margin and for plate tectonic models. Journal of Geophysical Research. 106, 19207-19220.

Carey, S. and Sigurdsson, H., 1989. The intensity of plinian eruptions. Bulletin of Volcanology. 51, 28-40.

Carr, M.J., Feigenson, M.D., 2013. Volcanism and Geochemistry in Central America: Progress and Problems. Inside the Subduction Factory. 138, 1-22.

Carroll, M.R., and Webster, J.D., 1994. Solubilities of sulfur, noble gases, nitrogen, chlorine and fluorine in magmas. Review in Mineralogy. 30, 231-279.

Cashman, K.V., Sparks, R.S.J., Blundy, J.D., 2017. Vertically extensive and unstable magmatic systems: A unified view of igneous processes. Science. 355, eaag3055.

Cashman, K.V and Giordano, G., 2014. Calderas and magma reservoirs. Journal of Volcanology and Geothermal Research. 288, 28-45.

Chiodini, G., Cioni, R., Marini, L., Panichi, C., 1995. Origin of the fumarolic fluids of Vulcano Island, Italy and implications for volcanic surveillance. Bulletin of Volcanology. 57, 99-110.

Christopher, T.E., et al., 2015. Crustal-scale degassing due to magma system destabilization and magma-gas decoupling at Soufriere Hills Volcano, Montserrat. Geochemistry, Geophysics, Geosystems. 16, 2797-2811.

Danyushevsky, L.V., McNeill, A.W., Sobolev, A.V., 2002. Experimental and petrological studies of melt inclusions in phenocrysts from mantle-derived magmas: an overview of techniques, advantages, and complications. Chemical Geology. 183, 5-24.

de Moor, J.M., Aiuppa, A., Avard, G., Wehrmann, H., Dunbar, N., Muller, C., Tamburello, G., Giudice, G., Liuzzo, M., Moretti, R., Conde, V., Galle, B., 2016. Turmoil at Turrialba Volcano (Costa Rica): Degassing and eruptive processes inferred from high-frequency gas monitoring. Journal of Geophysical Research: Solid Earth. 121, 5761-5775.

DeMets, C., 2001. A new estimate for the present-day Cocos-Caribbean plate motion: Implications for slip along the Central American volcanic arc. Geophysical Research Letters. 28, 4043-4046.

Duan, Z., Zhang, Z., 2006. Equation of state of the H_2O, CO_2, and H_2O-CO_2 systems up to 10 GPa and 2573.15K: Molecular dynamics simulations with ab initio potential surface. Geochimica et Cosmochimica Acta. 70, 2311-2324.

Fischer, T.P., Ramirez, C., Mora-Amador, R.A., Hilton, D.R., Barnes, J.D., Sharp, Z.D., Le Brun, M., de Moor, J.M., Barry, P.H., Füri, E., Shaw, A.M., 2015. Temporal variations in fumarole gas chemistry at Poás volcano, Costa Rica. Journal of Volcanology and Geothermal Research. 294, 56-70.

Funk, J., Mann, P., McIntosh, K., Stephens, J., 2009. Cenozoic tectonics of the Nicaraguan depression, Nicaragua, and Median Trough, El Salvador, based on seismic-reflection profiling and remote-sensing data. GSA Bulletin. 121, 1491-1521.

Giggenbach, W.F., Goguel, R.L., 1989. Collection of Geothermal and Volcanic Water and Gas Discharges. Chemistry Division, Department of Scientific and Industrial Research Petone, New Zealand. CD 2401, 1-81.

Gudmundsson, A, 2014. Elastic energy release in giant earthquakes and eruptions. Frontiers in Earth Science. 2, 1-12.

Hill, G.J., et al., 2009. Distribution of melt beneach Mount St. Helens and Mount Adams inferred from magnetotelluric data. Nature Geoscience. 2, 785-789.

Holloway, J.R., Blank, J.G., 1994. Application of experimental results to C-O-H species in natural melts. Reviews in Mineralogy and Geochemistry, 30, 187-230.

Iacovino, K., 2015. Linking subsurface to surface degassing at active volcanoes: A thermodynamic model with applications to Erebus volcano. Earth and Planetary Science Letters. 431, 59-74.

King, P.L., Larsen, J.F., 2013. A micro-reflectance IR spectroscopy method for analyzing volatile species in basaltic, andesitic, phonolitic, and rhyolitic glasses. American Mineralogist. 98, 1162-1171.

Kiser, E., et al., 2016. Magma reservoirs from the upper crust to the Moho inferred from high-resolution Vp and Vs models beneath Mount St. Helens, Washington State, USA. Geology. 44, 411-414.

La Femina, P.C., and Dixon, T.H., 2002. Bookshelf faulting in Nicaragua. Geology. 30, 751-754.

Lopez, T., Aguilera, F., Tassi, F., de Moor, J.M., Bobrowski, N., Aiuppa, A., Tamburerllo, G., Rizzo, A.L., Liuzzo, M., Viveiros, F., Cardellini, C., Silva, C., Fischer, T., Jean-Baptiste, P., Kazayaha, R., Hidalgo, S., Malowany, K., Lucic, G., Bagnato, E., Bergsson, B., Reath, K., Liotta, M., Carn, S., Chiodini, G., 2018. New insights into the magmatic-hydrothermal system and volatile budget of Lastarria volcano, Chile: Integrated results from the 2014 IAVCEI CCVG 12th Volcanic Gas Workshop. Geosphere. 14, 1-25.

Lowenstern, J.B., 1995. Application of silicate-melt inclusions to the study of magmatic volatiles. In J.F.H. Thompson, Ed., Magmas, Fluids and Ore Deposits. 23, 71-100.

Lowenstern, J.B., Pitcher, B.W., 2013. Analysis of H_2O in silicate glass using attenuated total reflectance (ATR) micro-FTIR spectroscopy. American Mineralogist. 98, 1660-1668.

MacQueen, P., Zurek, J., Williams-Jones, G., 2016. Connected magma plumbing system between Cerro Negro and El Hoyo Complex, Nicaragua revealed by gravity survey. Journal of Volcanology and Geothermal Research. 327, 375-384.

Madonia, P., Rizzo, A.L., Diliberto, I.S., Favara, R., 2013. Continuous monitoring of fumarole temperatures at Mount Etna (Italy). Journal of Volcanology and Geothermal Research. 257, 12-20.

Malilay, J., Real, M.G., Vanegas, A.R., Noji, E., Sinks, T., 1996. Public Health Surveillance after a Volcanic Eruption: Lessons from Cerro Negro, Nicaragua, 1992. Bulletin of PAHO. 30, 218-226.

McKnight, S.B., and Williams, S.N., 1997. Old cinder cone or young composite volcano?: The nature of Cerro Negro, Nicaragua. 4, 339-342.

McKnight, S.B., 1995. Eruptive History and Morphometric Evolution of a Young Composite Volcano: Cerro Negro, Nicaragua. MS Thesis. Arizona State University. Web. 13 April. 2017.

Metrich, N., Wallace, P.J., 2008. Volatile abundances in basaltic magmas and their degassing paths tracked by melt inclusions. Reviews in Mineralogy and Geochemistry. 69, 363-402.

Moore, L.R., Gazel, E., Tuohy, R., Lloyd, A.S., Esposito, R., Steele-MacInnis, M., Hauri, E.H., Wallace, P.J., Plank, T., Bodnar, R.J., 2015. Bubbles matter: An assessment of the contribution of vapor bubbles to melt inclusion volatile budgets. American Mineralogist. 100, 806-823.

National Academies of Science, Engineering, and Medicine. 2017. Volcanic Eruptions and Their Repose, Unrest, Precursors, and Timing. Washington, DC: The National Academies Press. doi: https://doi.org/10.17226/24650.

Newman, S., Lowenstern, J.B., 2001. VolatileCalc: a silicate melt-H_2O-CO_2 solution model written in Visual Basic for excel. Computers & Geosciences. 28, 597-604.

O'Dwyer, M., Padgett, M.J., McGonigle, A.J.S., Oppenheimer, C., Inguaggiato, S., 2003. Real-time measurement of volcanic H_2S and SO_2 concentrations by UV spectroscopy. Geophysical Research Letters. 30, 54-1, 54-4.

Patanè, D., Aiuppa, A., Aloisi, M., Behncke, B., Cannata, A., Coltelli, M., Di Grazia, G., Gambino, S., Gurrieri, S., Mattia, M., Salerno, G., 2013. Insights into magma and fluid transfer at Mount Etna by a multiparametric approach: A model of the events leading to the 2011 eruptive cycle. Journal of Geophysical Research: Solid Earth. 118, 3519-3539.

Patino, L.C., Carr, M.J., Feigenson, M.D., 2000. Local and regional variations in Central American arc lavas controlled by variations in subducted sediment input. Contributions to Mineral Petrology. 138, 265-283.

Power, J.A., Stihler, S.D., White, R.A., Moran, S.C., 2004. Observations of deep long-period (DLP) seismic events beneath Aleutian arc volcanoes, 1989-2002. Journal of Volcanology and Geothermal Research. 138, 243-266.

Roberts, T.J., Lurton, T., Giudice, G., Liuzzo, M., Aiuppa, A, Coltelli, M., Vignelles, D., Salerno, G., Coute, B., Chartier, M., Baron, R., Saffell, J.R., Scaillet, B., 2017. Validation of a novel Multi-Gas sensor for volcanic HCl alongside H_2S and SO_2 at Mt. Etna. Bulletin of Volcanology. 79, 1-14.

Roedder, E., 1984. Fluid Inclusions. Review of Mineralogy. 12, 644.

Roedder, E., 1979. Origin and significance of magmatic inclusions. Bulletin de Mineralogie. 102 467-510.

Roggensack, K., Hervig, R.L., McKnight, S.B., Williams, S.N., 1997. Explosive Basaltic Volcanism from Cerro Negro Volcano: Influence of Volatiles on Eruptive Style. Science. 277, 1639-1642.

Roggensack, K., 2001. Sizing up crystals and their melt inclusions: a new approach to crystallization studies. Earth and Planetary Science Letters. 187, 221-237.

Steele-MacInnis, M., Esposito, R., Bodnar, R.J., 2011. Thermodynamic model for the effect of post-entrapment crystallization on the H_2O-CO_2 systematics of vapor-saturated, silicate melt inclusions. Journal of Petrology. 52, 2461-2482.

Symonds, R.B., Gerlach, T.M., Reed, M.H., 2001. Magmatic gas scrubbing: implications for volcano monitoring. Journal of Volcanology and Geothermal Research. 108, 303-341.

Syracuse, E.M., Abers, G.A., Fischer, K., MacKenzie, L., Rychert, C., Protti, M., González, V, Strauch, W., 2008. Seismic tomography and earthquake locations in the Nicaraguan and Costa Rican upper mantle. Geochemistry, Geophysics, Geosystems. 9, 1-22.

Taran, Y., Zelenski, M., Chaplygin, I., Malik, N., Campion, R., Inguaggiato, S., Pokrovsky, B., Kalacheva, E., Melnikov, D., Kazahaya, R., Fischer, T., 2018. Gas Emissions from Volcanoes of the Kuril Island Arc (NW Pacific): Geochemistry and Fluxes. Geochemistry, Geophysics, Geosystems. 19, 1859-1880.

Tucker, J.M., Hauri, E.H., Marske, J.P., Pietruszka, A.J., Garcia, M.O., Trusdell, F.A. (in review). 2018. A high carbon content in the Hawaiian mantle from olivine-hosted melt inclusions. Geochimica et Cosmochimica Acta.

Venugopal, S., Moune, S., Williams-Jones, G., 2016. Investigating the subsurface connection beneath Cerro Negro volcano and the El Hoyo Complex, Nicaragua. Journal of Volcanology and Geothermal Research. 325, 211-224.

Wallace, P.J., 2005. Volatiles in subduction zone magmas: concentration and fluxes based on melt inclusion and volcanic gas data. Journal of Volcanology and Geothermal Research. 140, 217-240.

Wallace, P.J., Kamenetsky, V.S., Cervantes, P., 2015. Melt inclusion CO_2 contents, pressures of olivine crystallization, and the problem of shrinkage bubbles. American Mineralogist. 100, 787-794.

Ward, K.M., Zandt, G., Beck, S.L., Christensen, D.H., McFarlin, H., 2014. Seismic imaging of the magmatic underpinnings beneath the Altiplano-Puna volcanic complex from the joint inversion of surface wave dispersion and receiver functions. Earth and Planetary Science Letters. 404, 43-53.

Werner, C., Kelly, P.J., Doukas, M., Lopez, T., Pfeffer, M., McGimsey, R., Neal, C., 2013. Degassing of CO_2, SO_2, and H_2S associated with the 2009 eruption of Redoubt Volcano, Alaska. Journal of Volcanology and Geothermal Research. 259, 270-284.

Wotzlaw, J.F., Binderman, I.N., Stern, R.A., D'Abzac, F.X., Schaltegger, U., 2015. Rapid heterogeneous assembly of multiple magma reservoirs prior to Yellowstone supereruptions. Nature, Scientific Reports. 5, 1-10.

Appendix A

FTIR Spectra

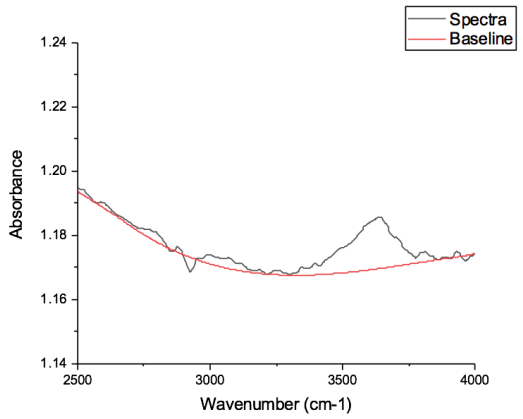

4-1 H_2O FTIR Spectra

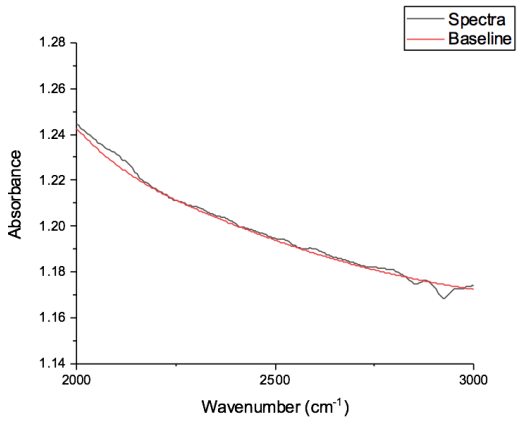

4-1 CO_2 FTIR Spectra

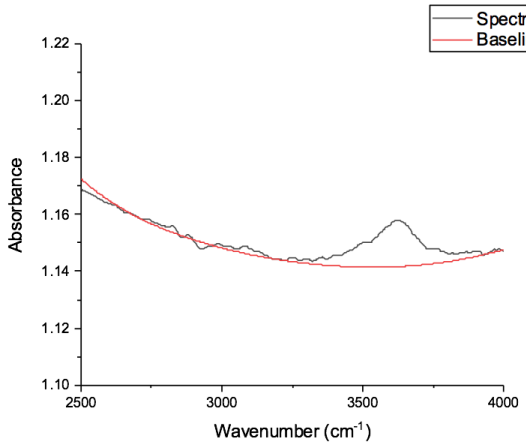

4-1b H_2O FTIR Spectra

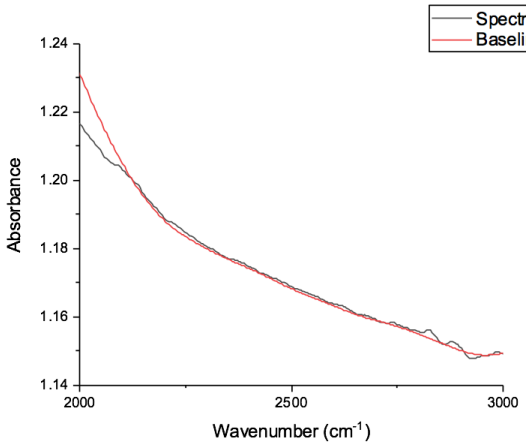

4-1b CO_2 FTIR Spectra

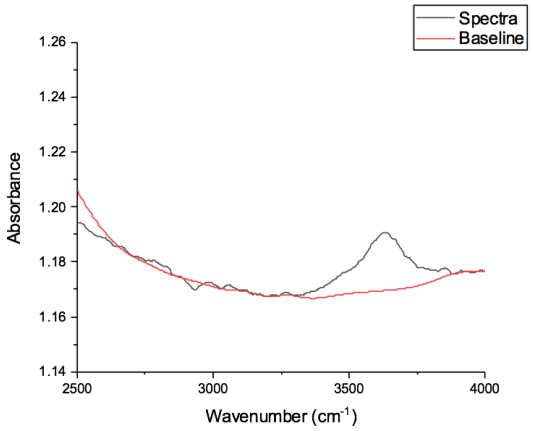

4-1c H_2O FTIR Spectra

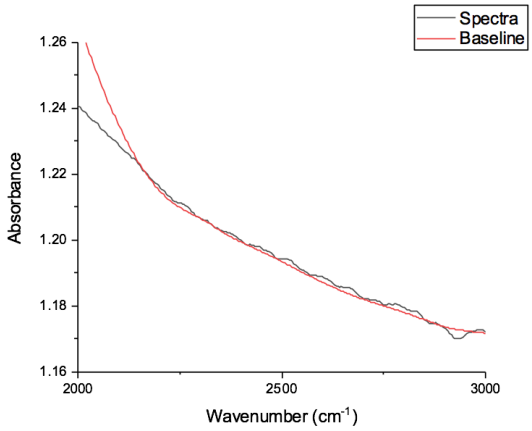

4-1c CO_2 FTIR Spectra

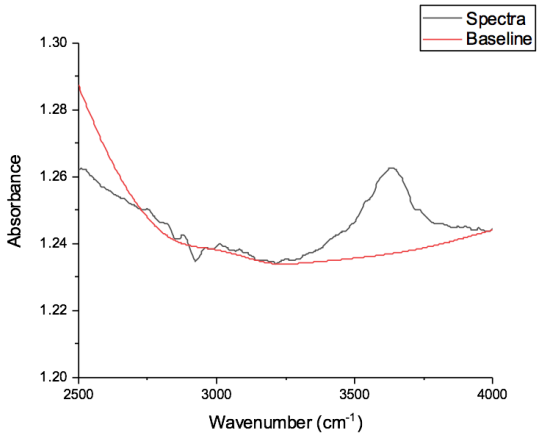

4-1a Rotated 180° H_2O FTIR Spectra

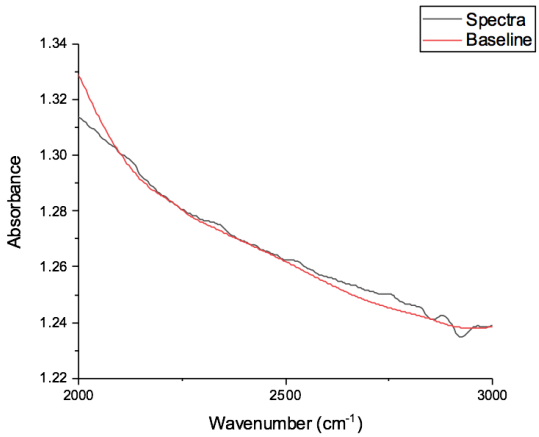

4-1a Rotated 180° CO_2 FTIR Spectra

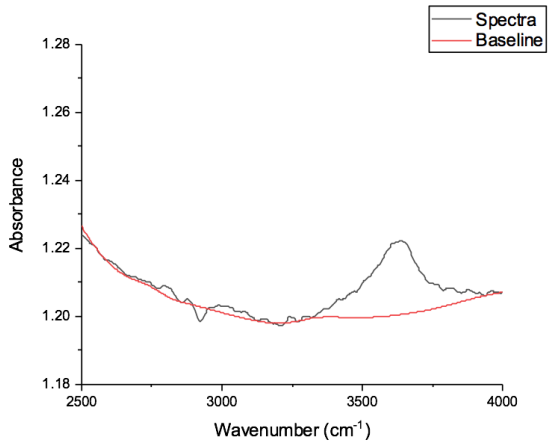

4-1b Rotated 180° H_2O FTIR Spectra

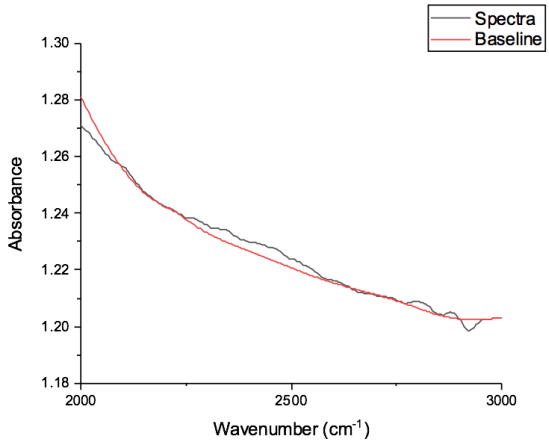

4-1b Rotated 180° CO_2 FTIR Spectra

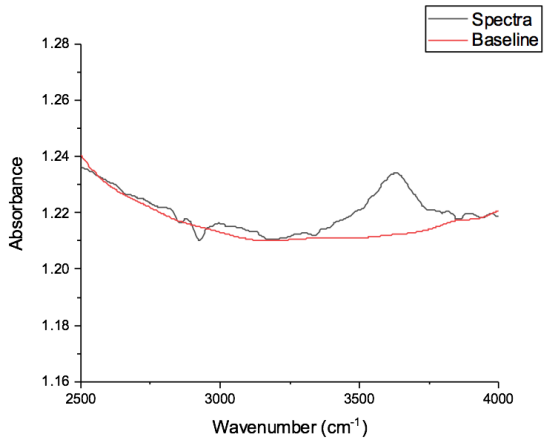

4-1c Rotated 180° H_2O FTIR Spectra

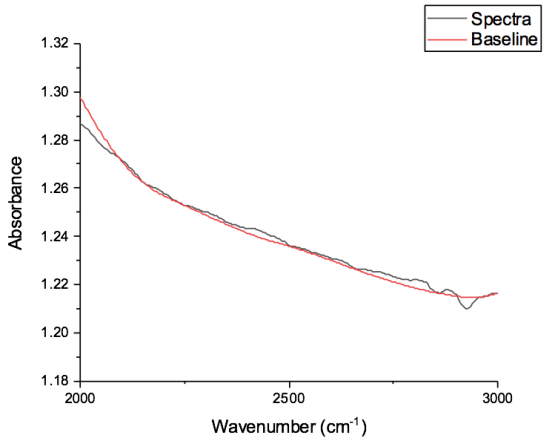

4-1c Rotated 180° CO_2 FTIR Spectra

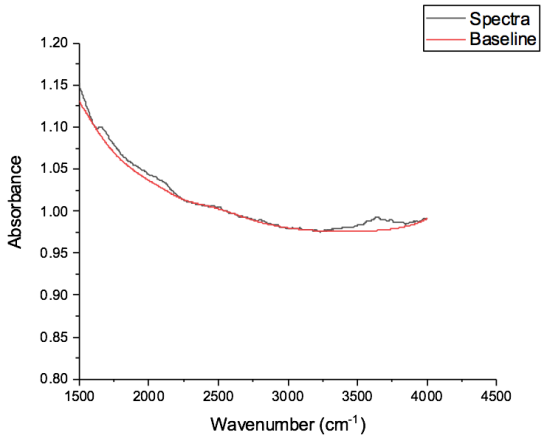

4-5a H_2O FTIR Spectra

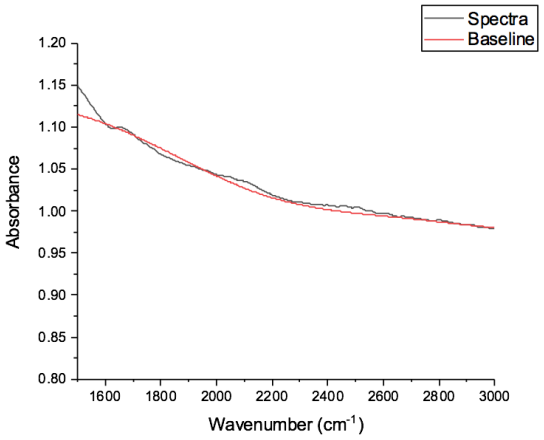

4-5a CO_2 FTIR Spectra

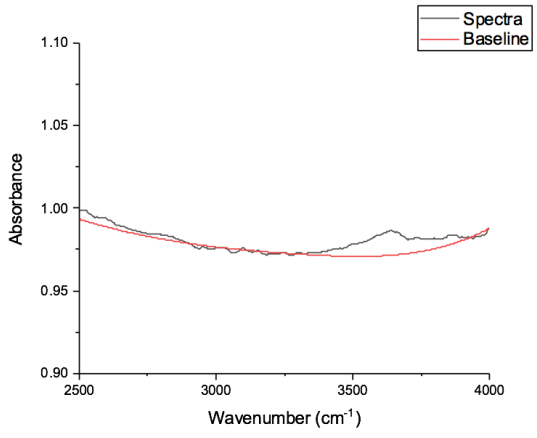

4-5b H_2O FTIR Spectra

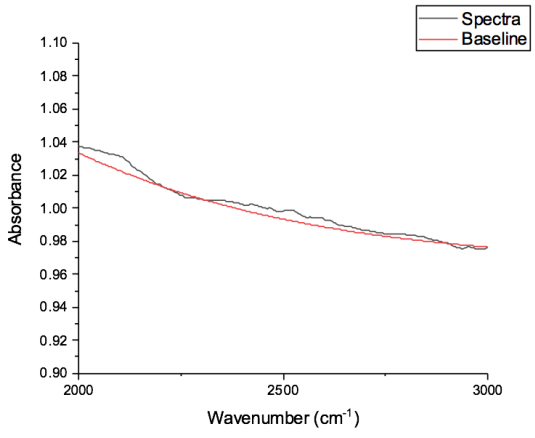

4-5b CO_2 FTIR Spectra

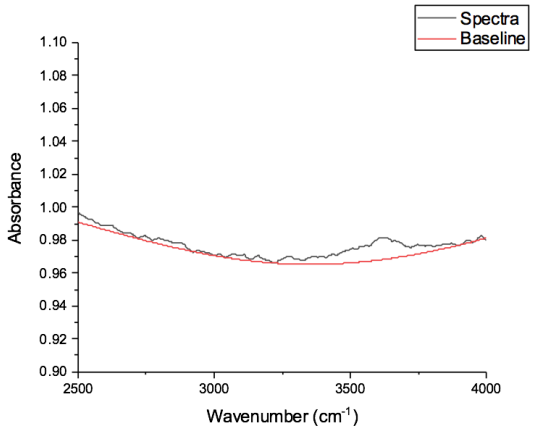

4-5c H_2O FTIR Spectra

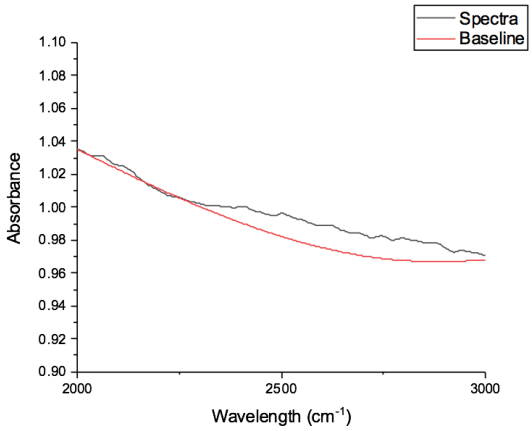

4-5c CO_2 FTIR Spectra

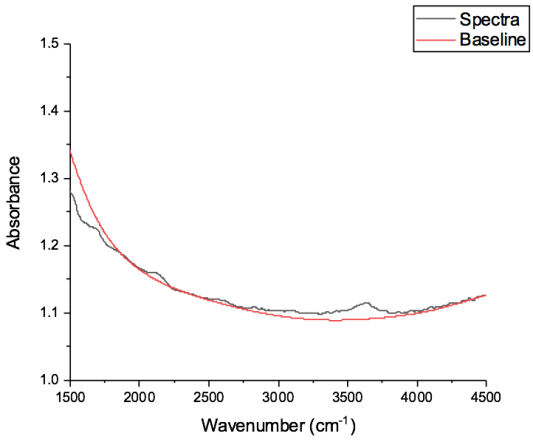

4-7a H_2O FTIR Spectra

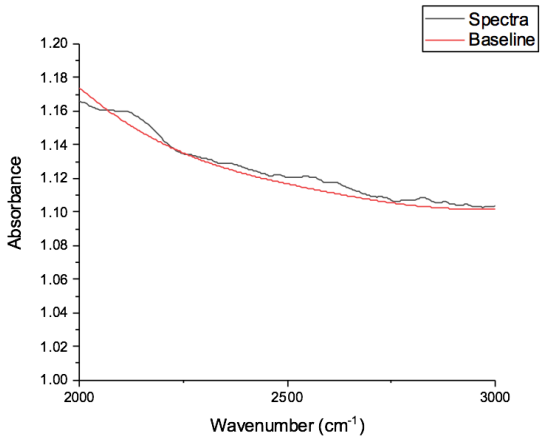

4-7a CO_2 FTIR Spectra

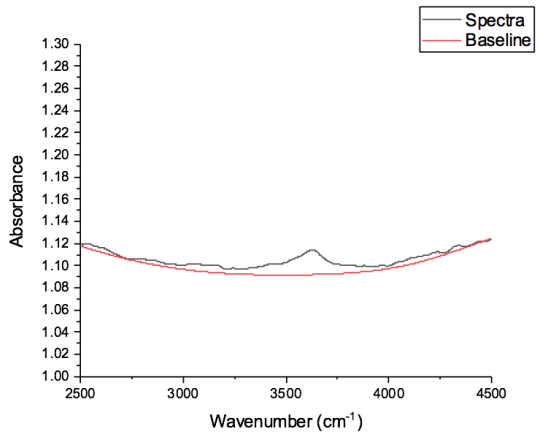

4-7b H_2O FTIR Spectra

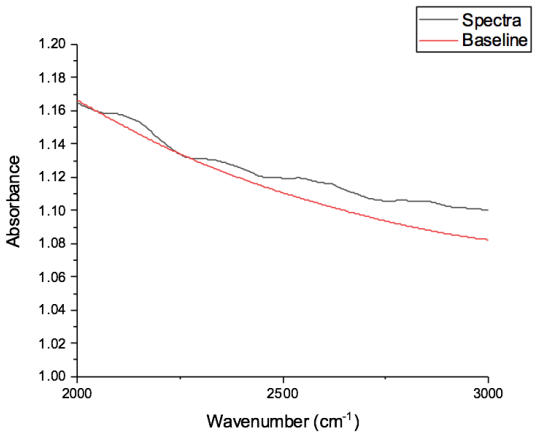

4-7b CO_2 FTIR Spectra

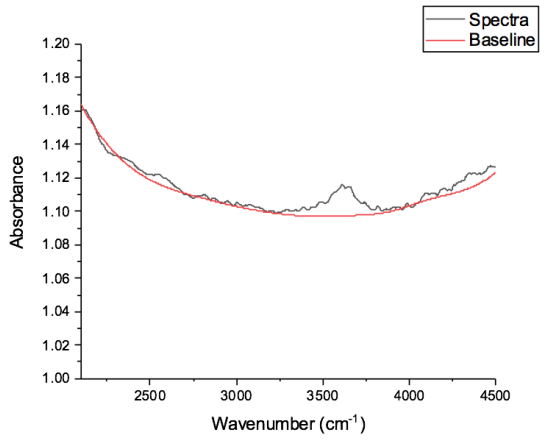

4-7c H_2O FTIR Spectra

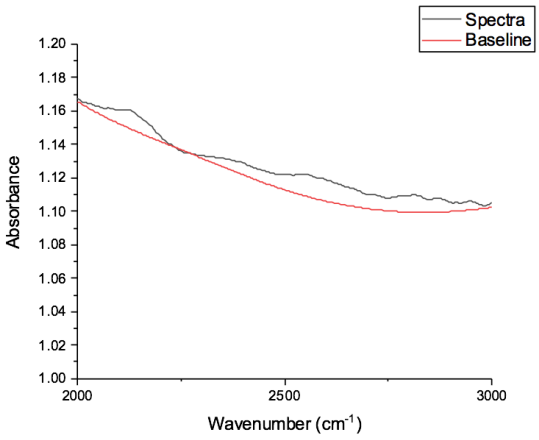

4-7c CO_2 FTIR Spectra

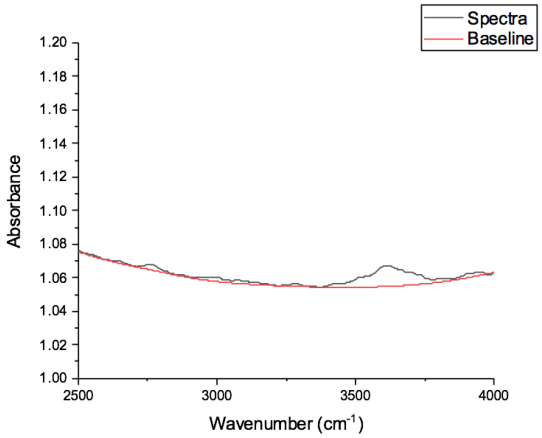

4-8a H_2O FTIR Spectra

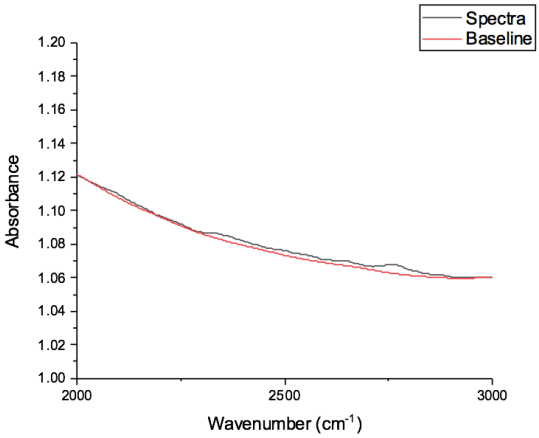

4-8a CO_2 FTIR Spectra

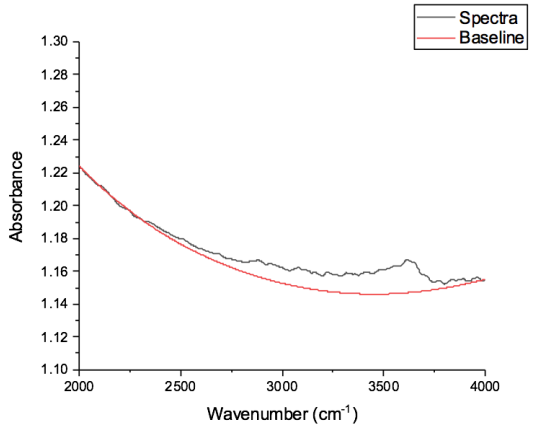

5-1a H_2O FTIR Spectra

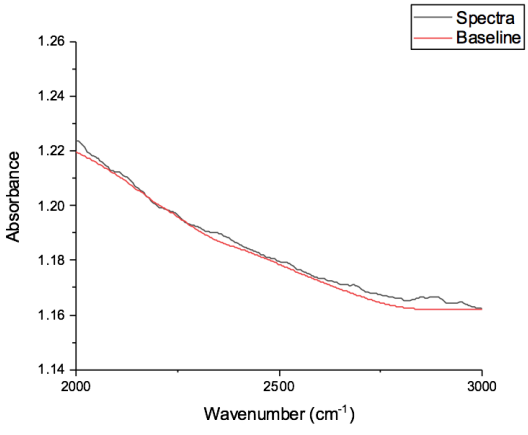

5-1a CO_2 FTIR Spectra

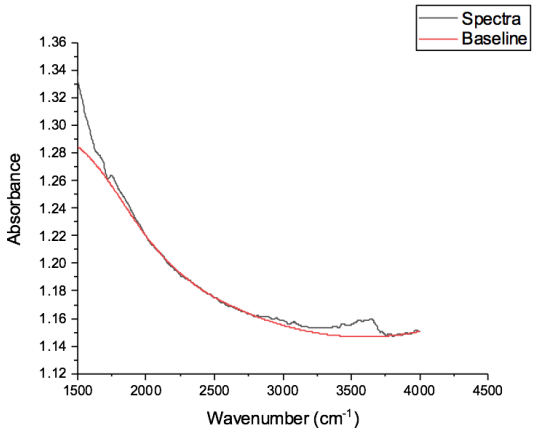

5-1b H_2O FTIR Spectra

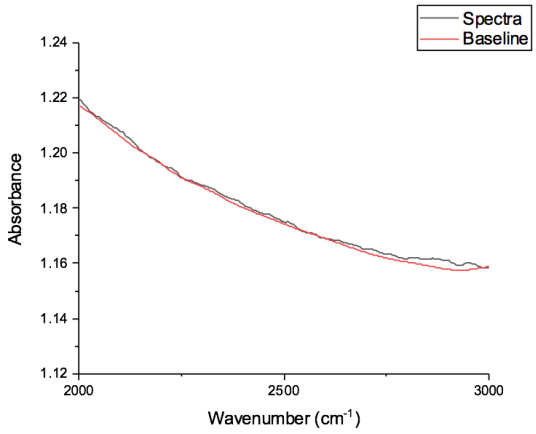

5-1b CO_2 FTIR Spectra

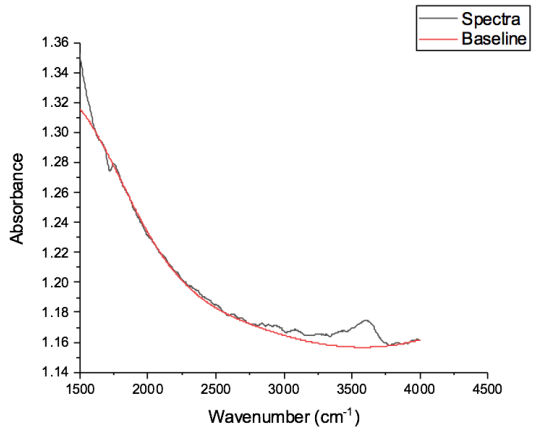

5-1c H_2O FTIR Spectra

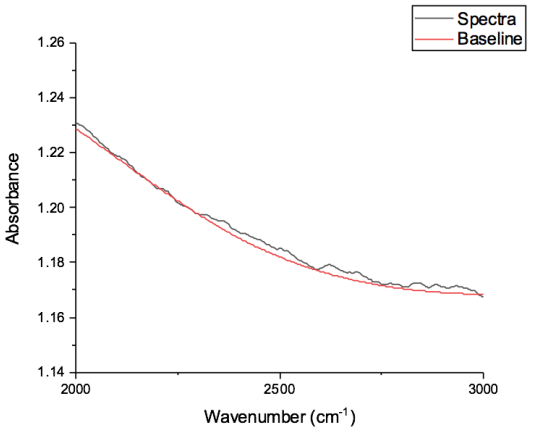

5-1c CO_2 FTIR Spectra

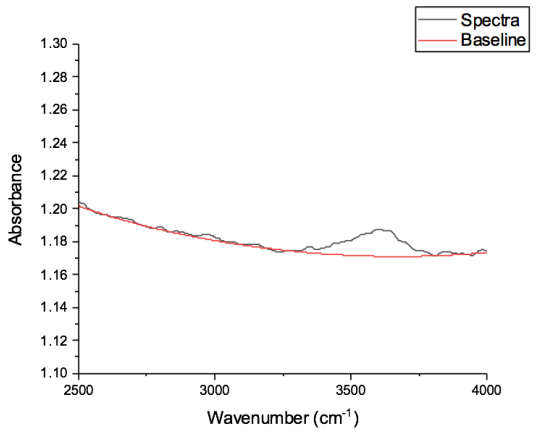

5-3a H_2O FTIR Spectra

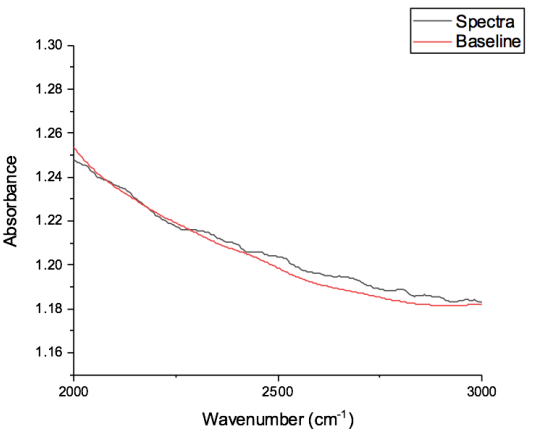

5-3a CO_2 FTIR Spectra

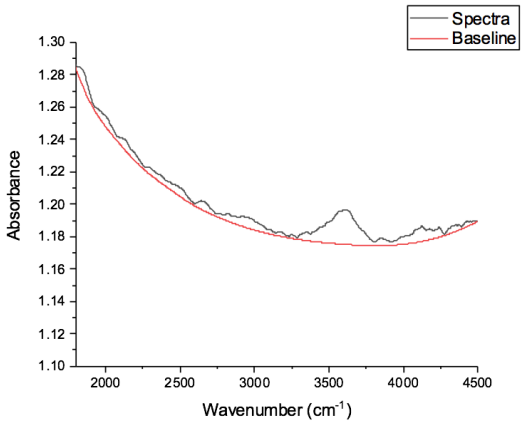

5-3b H_2O FTIR Spectra

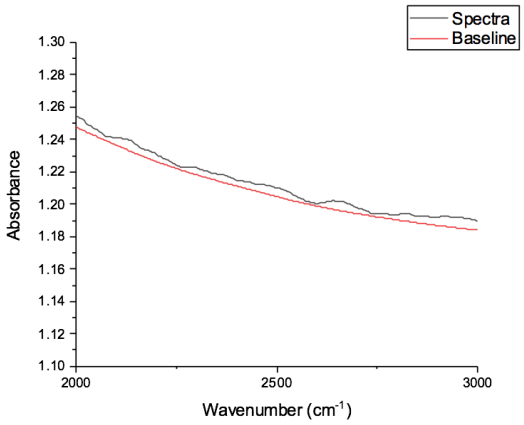

5-3b CO_2 FTIR Spectra

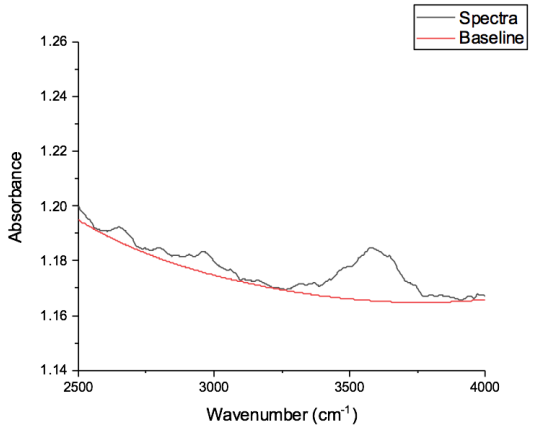

5-3c H_2O FTIR Spectra

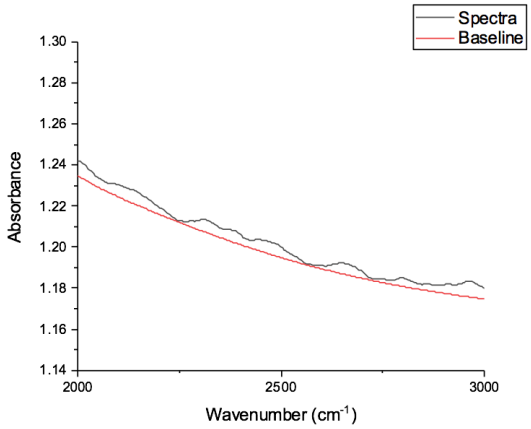

5-3c CO_2 FTIR Spectra

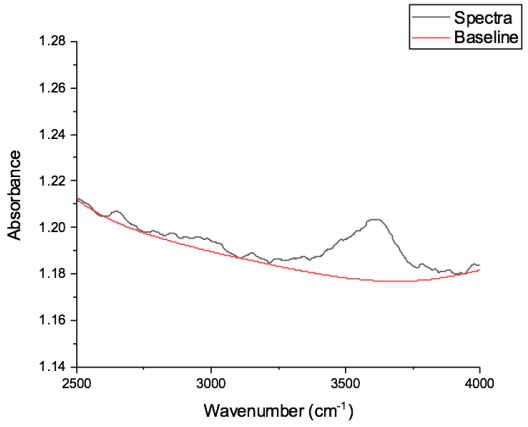

5-3a Rotated 180° H_2O FTIR Spectra

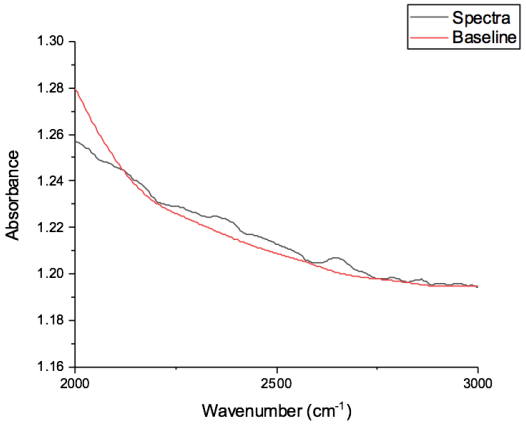

5-3a Rotated 180° CO_2 FTIR Spectra

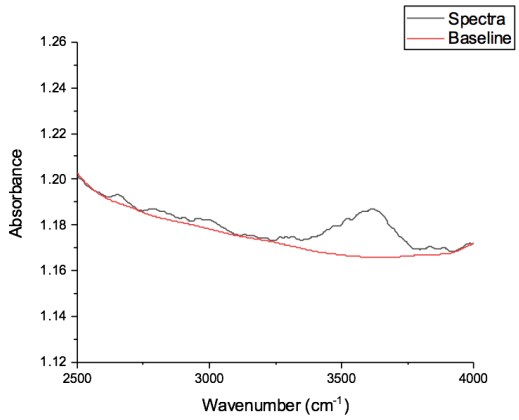

5-3b Rotated 180° H_2O FTIR Spectra

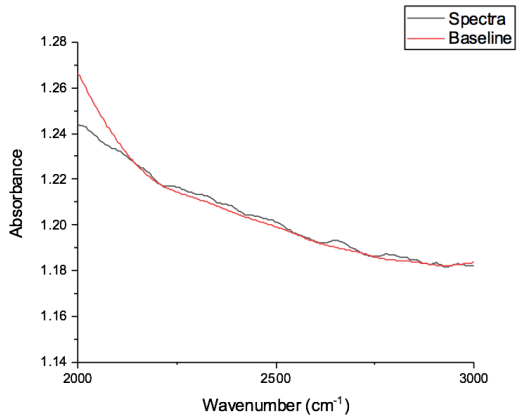

5-3b Rotated 180° CO_2 FTIR Spectra

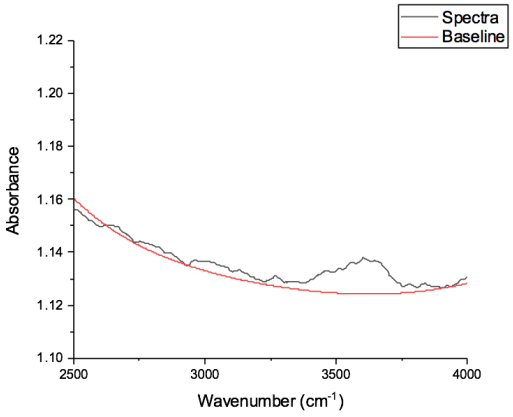

5-3c Rotated 180° H_2O FTIR Spectra

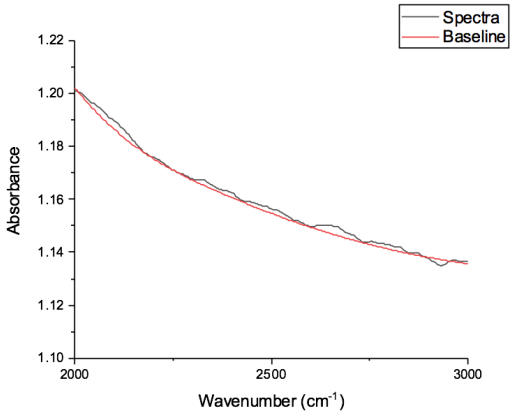

5-3c Rotated 180° CO_2 FTIR Spectra

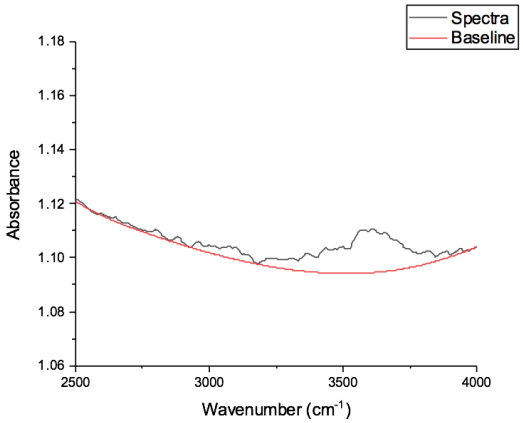

5-5a H_2O FTIR Spectra

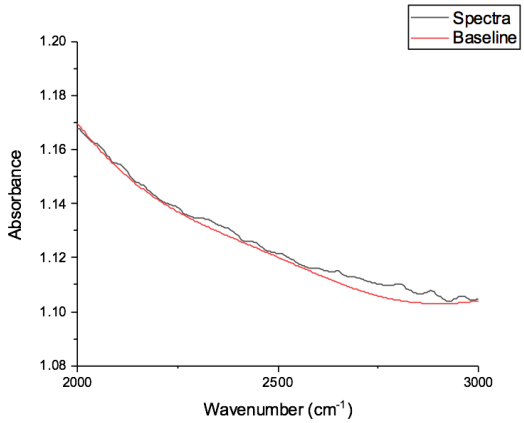

5-5a CO_2 FTIR Spectra

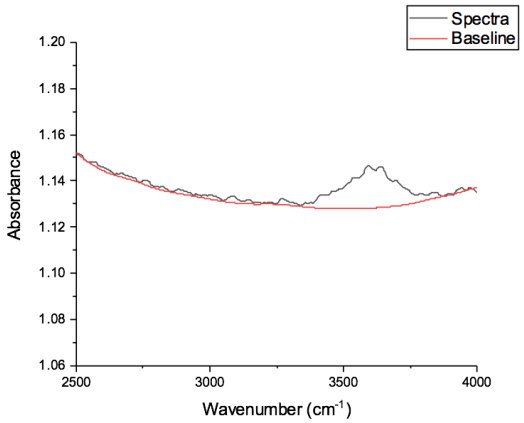

5-5b H_2O FTIR Spectra

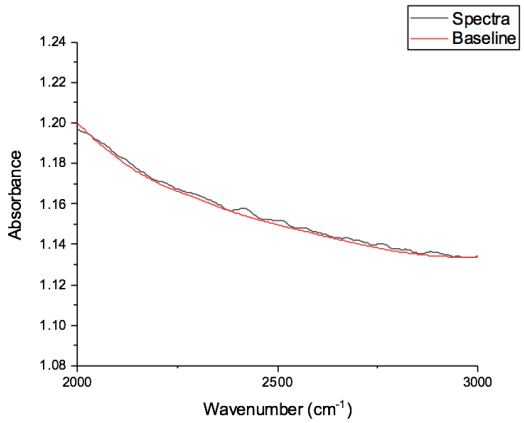

5-5b CO_2 FTIR Spectra

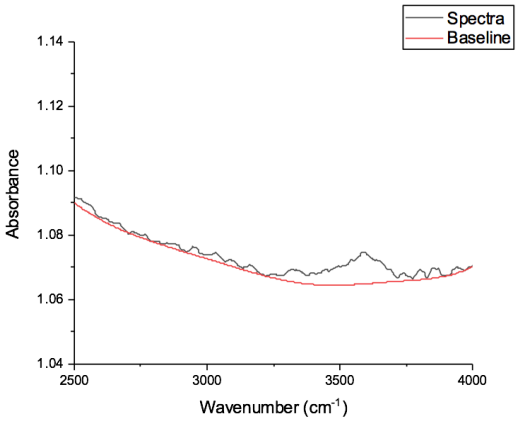

5-5c H_2O FTIR Spectra

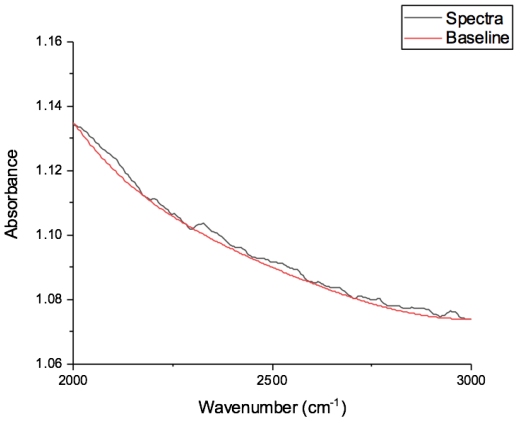

5-5c CO_2 FTIR Spectra

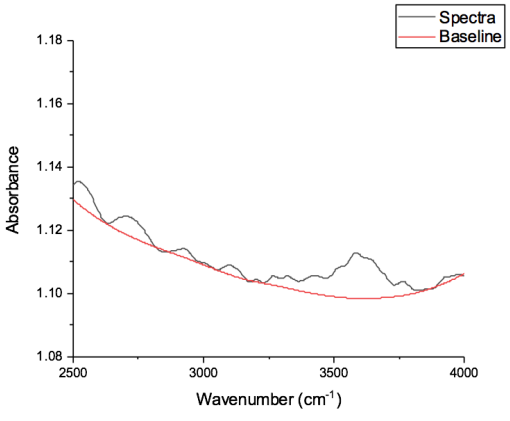

5-7a H_2O FTIR Spectra

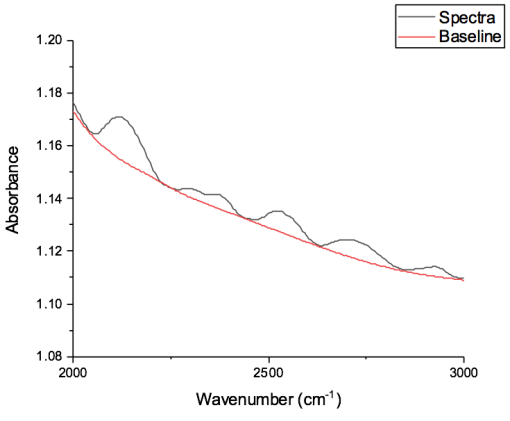

5-7a CO_2 FTIR Spectra

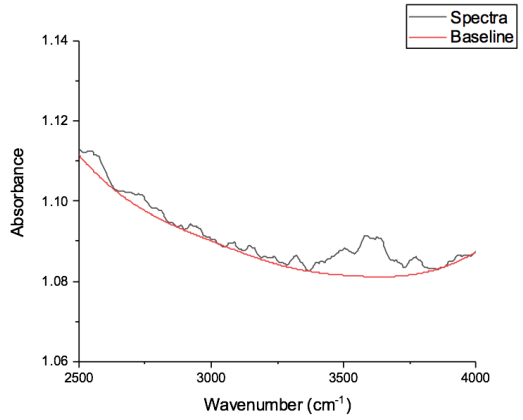

5-7b H_2O FTIR Spectra

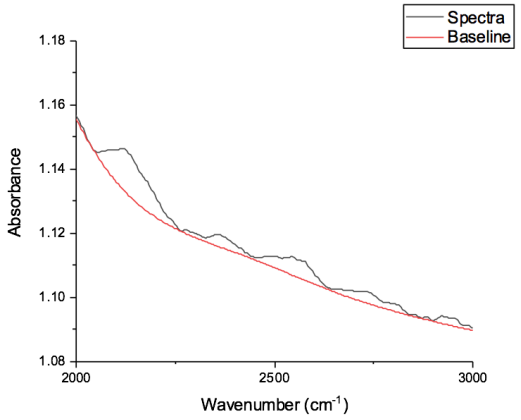

5-7b CO_2 FTIR Spectra

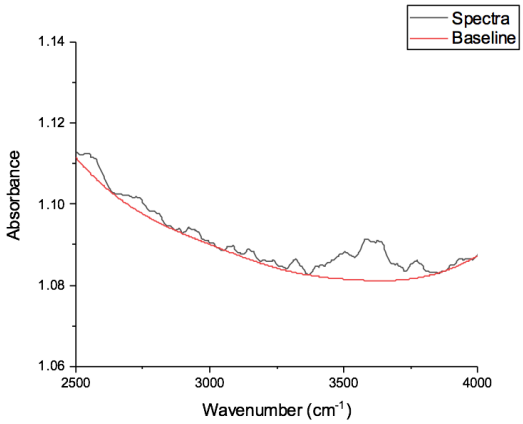

5-7c H_2O FTIR Spectra

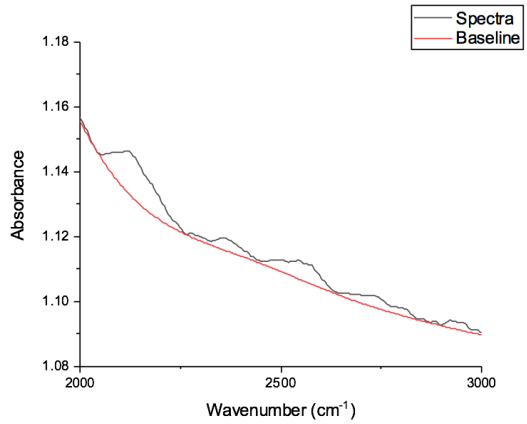

5-7c CO_2 FTIR Spectra

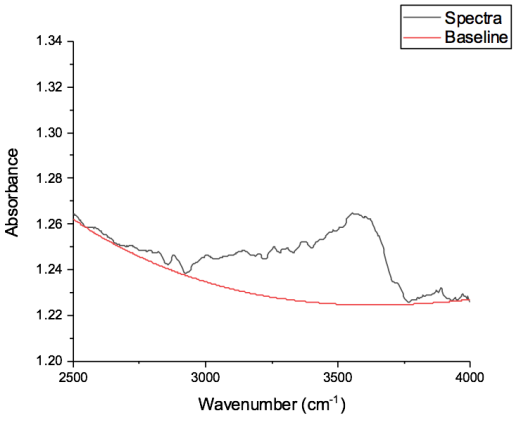

5-8a H_2O FTIR Spectra

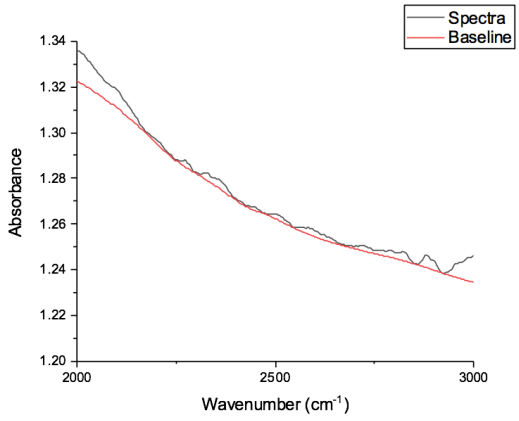

5-8a CO_2 FTIR Spectra

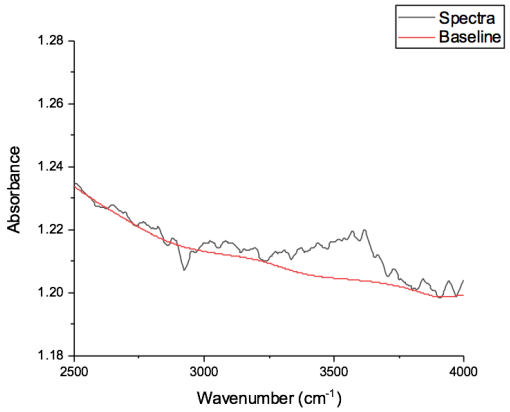

5-8b H_2O FTIR Spectra

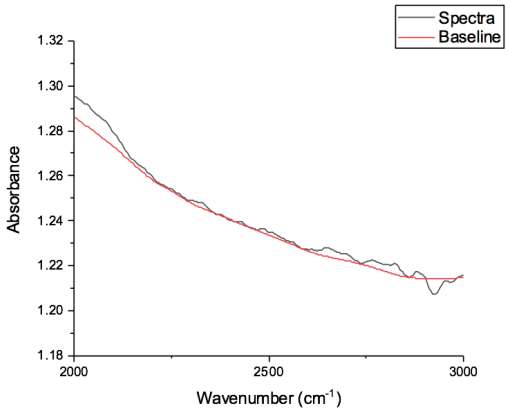

5-8b CO_2 FTIR Spectra

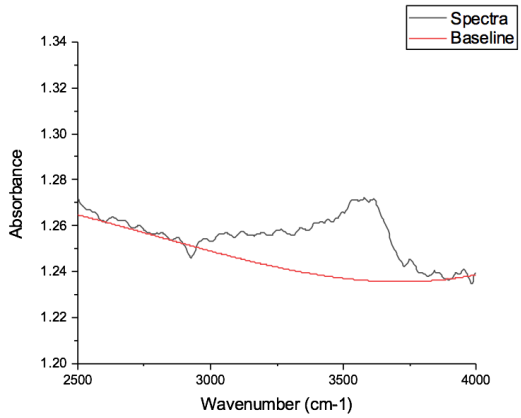

5-8c H_2O FTIR Spectra

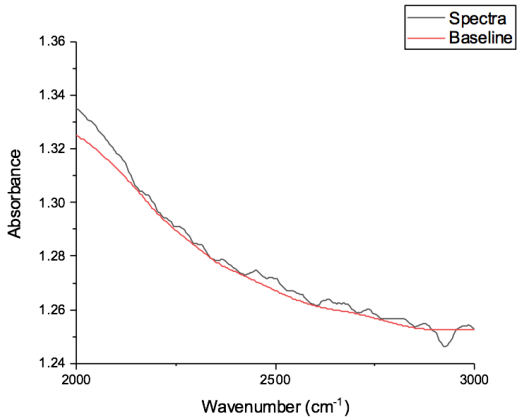

5-8c CO_2 FTIR Spectra

FTIR Peak Heights and Volatile Concentrations

Water	Y-Base	Y-Peak	H2O wt%
4-1a	1.1697	1.1858	2.01
4-1b	1.1417	1.1581	2.04
4-1c	1.1697	1.1908	2.64
4-5a	0.9772	0.9937	2.05
4-5b	0.9718	0.9868	1.87
4-5c	0.9683	0.9817	1.68
4-7a	1.0913	1.1152	2.99
4-7b	1.0922	1.1145	2.79
4-7c	1.0975	1.1160	2.31
4-8a	1.0548	1.0672	1.55
4-8b	0.8850	0.9035	2.31
4-8c	0.8810	0.9030	2.75
5-1a	1.1473	1.1669	2.46
5-1b	1.1468	1.1601	1.67
5-1c	1.1569	1.1750	2.27
5-3a	1.1712	1.1878	2.07
5-3b	1.1752	1.1967	2.69
5-3c	1.1655	1.1848	2.42
5-5a	1.0946	1.1107	2.02
5-5b	1.1286	1.1463	2.21
5-5c	1.0649	1.0748	1.24
5-7a	1.0986	1.1130	1.80
5-7b	1.0812	1.0910	1.23
5-7c	1.0927	1.1070	1.79
4-1a (Rotated)	1.2371	1.2626	3.19
4-1b (Rotated)	1.2006	1.2222	2.71
4-1c (Rotated)	1.2124	1.2345	2.76
5-3a (Rotated)	1.1771	1.2031	3.25
5-3b (Rotated)	1.1660	1.1872	2.65
5-3c (Rotated)	1.1242	1.1379	1.71
5-8a (Rotated)	1.2246	1.2635	4.86
5-8b (Rotated)	1.2038	1.2200	2.03
5-8c (Rotated)	1.2360	1.2715	4.44

Table 1 - Peak baselines and heights for each melt inclusion analysis for water content calculations.

Carbon Dioxide	Y-Base	Y-Peak	CO_2 (ppm)
4-1a	1.2039	1.2049	36.84
4-1b	1.1764	1.1770	20.00
4-1c	1.2015	1.2024	35.79
4-5a	1.0048	1.0081	126.32
4-5b	1.0021	1.0047	96.84
4-5c	0.9967	1.0014	176.84
4-7a	1.1250	1.1286	136.84
4-7b	1.1239	1.1295	208.42
4-7c	1.1269	1.1319	187.37
4-8a	1.0826	1.0858	120.00
4-8b	0.8370	0.8440	260.40
4-8c	0.8400	0.8460	223.20
5-1a	1.1873	1.1901	104.84
5-1b	1.1840	1.1850	35.37
5-1c	1.1919	1.1950	116.21
5-3a	1.2101	1.2128	97.89
5-3b	1.2148	1.2190	155.79
5-3c	1.2048	1.2095	173.47
5-5a	1.1298	1.1323	92.21
5-5b	1.1590	1.1602	45.47
5-5c	1.0988	1.1011	88.42
5-7a	1.1375	1.1415	147.79
5-7b	1.1163	1.1196	121.05
5-7c	1.1282	1.1339	210.53
4-1a (Rotated)	1.2736	1.2758	80.84
4-1b (Rotated)	1.2297	1.2339	157.89
4-1c (Rotated)	1.2473	1.2490	61.89
5-3a (Rotated)	1.2185	1.2249	237.26
5-3b (Rotated)	1.2094	1.2119	94.32
5-3c (Rotated)	1.1654	1.1674	74.53
5-8a (Rotated)	1.2768	1.2803	131.16
5-8b (Rotated)	1.2453	1.2478	91.37
5-8c (Rotated)	1.2765	1.2787	84.63

Table 2 - Peak baselines and heights for each melt inclusion analysis for carbon dioxide content calculations.

Appendix B

Microprobe Raw Data

	4-1	4-1	4-1	4-3	4-3	4-3
SiO2	48.90	48.71	48.92	46.82	47.11	46.55
TiO2	0.91	0.92	0.94	0.86	0.88	0.88
Al2O3	17.53	17.55	17.48	19.14	19.48	19.50
FeO	9.45	9.33	9.44	9.99	10.05	9.99
MnO	0.18	0.17	0.16	0.19	0.20	0.18
MgO	5.79	5.76	5.80	4.14	3.86	3.98
CaO	10.76	10.78	10.89	12.28	12.40	12.31
Na2O	0.42	0.43	0.43	0.67	0.74	0.72
K2O	0.38	0.36	0.38	0.28	0.29	0.29
P2O5	0.13	0.13	0.19	0.11	0.03	0.08
SO3	0.49	0.54	0.59	0.47	0.48	0.41
Cl	0.09	0.10	0.10	0.11	0.13	0.10
F	0.00	0.00	0.01	0.01	0.00	0.00
O	0.00	0.00	0.00	0.00	0.00	0.00
H2O	4.97	5.22	4.66	4.92	4.36	5.00
TOTAL	100.00	100.00	100.00	100.00	100.00	100.00

Table 1 - Raw oxide data for each of three spots analyzed on each melt inclusion. Sample 5-3 not included due to inability to locate the melt inclusion on the microprobe.

	4-5	4-5	4-5	4-7	4-7	4-7
SiO2	47.37	47.08	47.36	46.25	46.64	46.72
TiO2	1.03	1.07	1.08	0.77	0.75	0.81
Al2O3	18.74	18.22	18.75	16.39	16.45	16.41
FeO	9.86	10.17	9.83	11.67	11.61	11.68
MnO	0.19	0.20	0.20	0.22	0.22	0.21
MgO	3.57	4.10	3.66	6.00	6.08	5.81
CaO	10.27	10.29	10.17	10.82	10.90	10.92
Na2O	0.31	0.31	0.29	0.43	0.52	0.48
K2O	0.35	0.30	0.35	0.24	0.24	0.25
P2O5	0.13	0.22	0.22	0.12	0.08	0.16
SO3	0.75	0.71	0.65	0.29	0.34	0.35
Cl	0.11	0.08	0.10	0.11	0.08	0.07
F	0.00	0.00	0.01	0.00	0.00	0.00
O	0.00	0.00	0.00	0.00	0.00	0.00
H2O	7.32	7.26	7.34	6.69	6.09	6.13
TOTAL	100.00	100.00	100.00	100.00	100.00	100.00

Table 1 continued - Raw oxide data for each of three spots analyzed on each melt inclusion. Sample 5-3 not included due to inability to locate the melt inclusion on the microprobe.

	4-8	4-8	4-8	5-1	5-1	5-1
SiO2	46.13	46.44	46.32	49.26	49.20	48.56
TiO2	0.80	0.83	0.85	1.11	1.11	1.13
Al2O3	17.79	17.96	17.83	15.93	16.07	15.87
FeO	10.26	10.20	10.20	12.15	12.05	12.06
MnO	0.19	0.19	0.16	0.22	0.25	0.24
MgO	5.19	5.07	5.17	4.97	5.52	5.26
CaO	12.02	12.00	11.95	9.95	9.66	9.84
Na2O	0.53	0.55	0.50	0.53	0.51	0.50
K2O	0.27	0.29	0.29	0.52	0.52	0.51
P2O5	0.09	0.14	0.11	0.14	0.10	0.13
SO3	0.42	0.38	0.46	0.29	0.26	0.16
Cl	0.08	0.07	0.07	0.12	0.12	0.11
F	0.00	0.00	0.00	0.00	0.00	0.00
O	0.00	0.00	0.00	0.00	0.00	0.00
H2O	6.21	5.90	6.07	4.80	4.64	5.62
TOTAL	100.00	100.00	100.00	100.00	100.00	100.00

Table 1 continued - Raw oxide data for each of three spots analyzed on each melt inclusion. Sample 5-3 not included due to inability to locate the melt inclusion on the microprobe.

	5-5	5-5	5-5	5-7	5-7	5-7
SiO2	49.07	49.27	49.20	48.25	48.72	48.39
TiO2	1.00	1.01	1.01	0.84	0.85	0.83
Al2O3	16.55	16.55	16.47	18.16	18.07	18.05
FeO	12.19	12.18	12.20	9.97	9.92	9.90
MnO	0.20	0.22	0.22	0.17	0.20	0.18
MgO	5.75	5.74	5.72	5.34	5.27	5.42
CaO	9.63	9.63	9.74	11.52	11.66	11.62
Na2O	0.47	0.48	0.45	0.33	0.37	0.37
K2O	0.36	0.32	0.35	0.28	0.29	0.29
P2O5	0.12	0.08	0.09	0.10	0.11	0.10
SO3	0.50	0.49	0.51	0.34	0.37	0.37
Cl	0.07	0.11	0.08	0.10	0.08	0.10
F	0.01	0.00	0.00	0.00	0.00	0.01
O	0.00	0.00	0.00	0.00	0.00	0.00
H2O	4.09	3.91	3.97	4.60	4.10	4.37
TOTAL	100.00	100.00	100.00	100.00	100.00	100.00

Table 1 continued - Raw oxide data for each of three spots analyzed on each melt inclusion. Sample 5-3 not included due to inability to locate the melt inclusion on the microprobe.

	5-8	5-8	5-8
SiO2	48.08	48.56	48.54
TiO2	0.88	0.90	0.87
Al2O3	18.76	18.71	18.86
FeO	9.00	9.08	9.08
MnO	0.15	0.15	0.18
MgO	4.93	4.87	4.91
CaO	11.50	11.34	11.41
Na2O	0.39	0.41	0.41
K2O	0.31	0.30	0.30
P2O5	0.18	0.17	0.20
SO3	0.41	0.44	0.40
Cl	0.05	0.07	0.08
F	0.00	0.03	0.00
O	0.00	0.00	0.00
H2O	5.37	4.97	4.76
TOTAL	100.00	100.00	100.00

Table 1 continued - Raw oxide data for each of three spots analyzed on each melt inclusion. Sample 5-3 not included due to inability to locate the melt inclusion on the microprobe.